A Grand Potential based Multi-Phase Field Model for Alloy Solidification

Kaushik Natarajan Shampur
Centre for the Physics of Materials
Department of Physics
McGill University
Montréal, Québec
Canada
April, 2017

A Thesis submitted to the Faculty of Graduate Studies and Research in partial fulfillment of the requirements for the degree of Master of Science

CONTENTS

	Ab	stract	•	VIII
	Rés	sumé		ix
	Sta	itemen	t of Originality	xi
	Acl	knowle	dgments	xii
1	In	TRODU	JCTION	1
		1.0.1	Single-order parameter phase field models	2
		1.0.2	Multi-order parameter phase field models	3
		1.0.3	Phase field models with an orientation order parameter	4
		1.0.4	Phase field models based on phase fraction fields	5
		1.0.5	Decoupling solute concentration from the order parameter through the interface	n 6
		1.0.6	Dealing with spurious interface kinetics caused by numerically diffuse interfaces	7
		1.0.7	Deriving phase field models in the grand canonical ensemble .	8
		1.0.8	Model developed in this thesis	9
	1.1	Paradi	igm of Two-Phase Solidification	10
	1.2	Use of	Adaptive Mesh Refinement in Phase Field modelling	12
	1.3	Outlin	ne of thesis	12
2	GF	RAND :	Potential Phase Field Model	15
	2.1	Grand	Potential Thermodynamics	15
	2.2	Grand	Potential Phase Field Functional	17

iv Contents

	2.2.1	Interaction between order parameters	19
	2.2.2	Properties of the single-phase grand potential $\omega^{\vartheta}({m \mu})$	19
	2.2.3	Concentration of a multi-phase system in the grand potential ensemble	20
2.3	Phase	Field Dynamics	22
	2.3.1	Traditional form	22
	2.3.2	Reformulation of phase field model dynamics in terms of ϕ and μ	23
	2.3.3	Order parameter equaitons	23
	2.3.4	Chemical potential equations	24
2.4	Equilil	orium Properties of Grand Potential Functional	25
	2.4.1	Equilibrium concentration field	26
	2.4.2	Equilibrium solid-liquid interfaces	26
	2.4.3	Equilibrium solid-solid interfaces	27
2.5	Non-V	ariational Dynamics for Diffuse Interfaces	28
2.6	Multi-	Phase Binary Alloy with Parabolic Free Energies	31
	2.6.1	Phase coexistence	31
	2.6.2	Grand potential of a phase, and multi-phase concentration and susceptibility	33
	2.6.3	Casting the phase field equations in terms of supersaturation .	34
2.7	Conne	ction to Previous Models	35
	2.7.1	Special case 1 : Pure material solidification	36
	2.7.2	Special case 2 : Polycrystalline dilute binary alloy solidification	36
	2.7.3	Recovering the Supersaturation Limit of [1]	37
2.8	Therm	al fluctuations in the phase field equations	39
	2.8.1	Non-dimensional form of the phase field equations	40

CONTENTS

		2.8.2	Simplification of the noise amplitude for the order parameter	4.1
		2.0.2	equation	41
		2.8.3	Calculation of the capillary length	42
	2.9	Interp	reting the role of λ in phase field modelling	43
		2.9.1	Interpreting the dual role of λ in the noise amplitude	45
3	RE	SULTS		47
	3.1	Phase	Diagram and Free Energy Construction	47
		3.1.1	Ideal binary eutectic alloy	47
		3.1.2	Silver-copper alloy system	48
	3.2	Lamel	lar Eutectic Structures	53
		3.2.1	qualitative features	53
		3.2.2	Numerical quantities used in simulations	56
	3.3	Homog	geneous Two-Phase Nucleation	58
		3.3.1	Implementation of order parameter noise	58
		3.3.2	Demonstration of homogeneous nucleation	59
		3.3.3	λ invariance in nucleation	60
4	C	ONCLU	JSIONS	63
I		HASE STEMS	FIELD DYNAMICS FOR GENERAL COMPLEX ALLOY	66
	A.1	Multi- Forms	Phase, Multi-Component Alloys with Quadratic Free Energy	66
E	3 In	ICORP	ORATING TEMPERATURE	77
	Ref	erence	S	81

LIST OF FIGURES

1.1	Experimental micrographs of regular and irregular eutectics: (a) regular Al-Au eutectic structure; (b) irregular Al-Si eutectic structure; (c) regular CBr ₄ C ₂ Cl ₆ ; (d) irregular borneol-SCN eutectic	11
1.2	(a) Example eutectic phase diagram; (b) example eutectic microstructure form solidification; (c) a close up look at the lamellar structures showing coupled $\alpha-\beta$ growth	11
3.1	Ideal symmetric phase diagram for a fictitious alloy. Horizontal axis is concentration of solute and on the vertical axis is the temperature. Regions below the orange and purple lines are single phase coexistence of two solids (α to the left and β to the right. Regions above the blue and yellow lines corresponds to liquid phase. The region between the orange and blue denoted coexistence between one α solid and the liquid and the region between the purple and yellow denote coexistence between β solid and the liquid	48
3.2	Parabolic free energies for fictitious alloy phases, at a specific temperature. Blue is α solid, yellow is β solid and orange is liquid. A simultaneously common tangent line to the blue and orange curves marks the concentrations of α solid (tangent to blue curve) and liquid (tangent to orange curve. A simultaneously common tangent line to the yellow and orange curves marks the concentrations of the β solid (tangent to yellow curve) and liquid (tangent to orange curve	49
3.3	Silver-copper phase diagram	50
3.4	Experimental free energy (purple and dark purple) overlaied with fitted parabolic free energies (other colours) At T = 1230 K	51
3.5	Comparison of how well the parabolic approximations are at two different temperatures. $T=1050~K~(left)$ and $T=1450~K~(right)$	52
3.6	Side by side comparison of experimental (right) and approximately reconstructed phase diagram (left). Temperature reconstruction range was lowered to T=1500 as that is the higher limit for the β side of the phase diagram. The liquidus lines in this (left) case are extended for their full metastable projection	52
3.7	K^{eff} vs Temperature curves. A look at the liquid to solid curvature ratios at different temperatures. Note the inflection at the Eutectic temperature, which is when the system transition from stable to metastable	53

List of Figures vii

3.8	Lamellar front comprised of α phase (red) and β phase growing into an undercooled liquid. An elimination event of an α lamella due to instability is shown $\sim 3/4$ up the vertical direction	54
3.9	Example concentration profile across a lamellar front where high concentration is the β solid phase (see text) and low concentration is the α solid phase	55
3.10	Linear scaling or inverse square distance $1/\lambda^2$ between two-phase lamella as a function of eutectic front speed ν^* . This result is consistent with the celebrated Jackson and Hunt scaling analysis [2]	55
3.11	Oscillation modes of lamella due to instability due to the minimum undercooling concept	56
3.12	Stable 3D growth of lamellae growing in on an adaptive mesh. Zoom in of the total system is shown	57
3.13	Top left to right, to bottom left to right: homogeneous nucleation of α (blue) at temperatures above the eutectic temperature, followed by inter-phase nucleation of $\beta(yellow)$. Parameter $\lambda=8.03$ and initial supersaturation of $U_{\alpha}\approx-0.21$. The dimensionless system size was $(1862\ \bar{x}/\bar{d_o})^2$ and the dimensionless time (scaled by $\bar{D}/\bar{d_o}^2$) was ≈ 35000 (top left), 79000(top right), 114000(bottom left), 158000(bottom right). Overbars represent scaling of space with W and time with τ	59
3.14	Solid fraction comparison in unscaled (left) and scaled (right) time, indicating the effect of λ as a convergence parameter, averaged over 20 runs for each λ	62
3.15	Left $\lambda = 14.7$, dimensionless time ≈ 47000 , dimensionless space $\approx 1867^2$. Right $\lambda = 8.03$, dimensionless time ≈ 45000 , dimensionless space $\approx 1862^2$. The higher λ 's concentration map is essentially a 'zoom' in of the lower λ because of the nature of λ 's spatial scaling	62
3.16		62

Abstract

The ability to model phase transitions in complex (i.e. multi-component and multi-phase) alloys, accurately, efficiently, and in an accessible manner, is important in material science. This thesis derives a new model that extends the quantitative model of polycrystalline solidification of Ofori-Opoku et al [3] to the case of multiple components and alloy phases through a grand potential functional description. Here, solidification is described by a set of order parameters describing solid phases and a set chemical potentials describing solute components. Solidification of a solid phase is driven by the grand potential difference between it and the liquid, expanded here to quadratic order in the chemical potential difference (relative to equilibrium) of each solute, i.e., its supersaturation. This allows us to model both near and far-from equilibrium solidification conditions, and to easily make contact with previous quantitative single-crystal phase field theories in the literature. Thermal fluctuations in the theory are treated via stochastic noise, a feature important for modelling multiphase nucleation self-consistently.

Working in the grand canonical ensemble treats the evolution of order parameter and chemical potential as a coupled process, unique compared to the traditional methods. As a result, complete decoupling of all diffusion fields and order parameter fields is achieved at equilibrium, making it possible to easily set solid-liquid or solid-solid interface energy independently of solute distribution across an an interface, an important feature for quantitative meso-scale calculations. Chemical diffusion equations in the model are augmented by a non-variational, so-called *anti-trapping* flux in each solute species. These fictitious fluxes are used in the literature in some phase field theories to correct for spurious solute trapping effects caused by the use of a diffuse interface, which is done solely for numerical expediency.

We demonstrate its workings of our model in the limit of a two-component eutectic alloy system simulated with 2D dynamic adaptive mesh refinement. Benchmark eutectic lamellar simulations and measurements are first performed. Following that, two-phase homogenous nucleation and growth are examined. In the limit of near-equilibrium interfaces (zero interface kinetics), we illustrate two-phase grain growth scaling that is independent of nucleation barrier.

Résumé

La capacité à modéliser des transitions de phase dans des alliages complexes (c'est-àdire multicouches et multiphases), de manière précise, efficace et accessible est importante dans la science des matériaux. Cette thèse dérive un nouveau modèle qui étend le modèle quantitatif de solidification polycristalline d'Ofori-Opoku et al [3] au cas de multiples composantes et phases d'alliage à travers une description fonctionnelle de grand potentiel. Ici, la solidification est décrite par un ensemble de paramètres d'ordre décrivant des phases solides et un ensemble de potentiels chimiques décrivant des composantes de soluté. La solidification d'une phase solide est entraînée par la grande différence de potentiel entre celle-ci et le liquide, étendue ici à l'ordre quadratique dans la différence de potentiel chimique (par rapport à l'équilibre) de chaque soluté, c'est-à-dire sa sursaturation. Ceci nous permet de modéliser à la fois des conditions de solidification proches et lointaines et de faire facilement le contact avec des théories de champ de phase monocristalline quantitatives précédentes dans la littérature. Les fluctuations thermiques de la théorie sont traitées par le bruit stochastique, une caractéristique importante pour la modélisation de la nucléation multi-phase de façon autonome.

Travailler dans le grand ensemble canonique traite l'évolution du paramètre d'ordre et du potentiel chimique comme un processus couplé, unique par rapport aux méthodes traditionnelles. Le découplage complet de tous les champs de diffusion et de paramètres d'ordre est ainsi obtenu à l'équilibre, ce qui permet de régler facilement l'énergie d'interface solide-liquide ou solide-solide indépendamment de la distribution de soluté à travers une interface, Calculs à l'échelle. Les équations de diffusion chimique dans le modèle sont augmentées par un flux non-variationnel, appelé antipiégeage dans chaque espèce de soluté. Ces flux fictifs sont utilisés dans la littérature dans certaines théories de champ de phase pour corriger les effets parasites parasites parasites causés par l'utilisation d'une interface diffuse, ce qui est fait uniquement pour l'opportunité numérique.

Nous démontrons son fonctionnement de notre modèle dans la limite d'un système d'alliage eutectique à deux composants simulé avec un raffinement en maillage adaptatif dynamique 2D. Des simulations et des mesures lamellaires eutectiques de

x List of Figures

référence sont d'abord effectuées. Ensuite, on examine la nucléation et la croissance homogènes en deux phases. Dans la limite des interfaces de quasi-équilibre (cinétique d'interface nulle), nous illustrons la mise à l'échelle en deux phases de la croissance du grain qui est indépendante de la barrière de nucléation.

Statement of Originality

The Masters Thesis consists of the derivation and benchmarking of a new grand potential phase field theory for multiple phase and multiple components, which builds on the ideas of Refs. [3, 4, 1]. My contributions include:

- Contributed to the theory of the multi-phase and multi-component model and verified all the theoretical derivations presented herein
- Computationally implemented and benchmarked two-phase properties of the model. I then incorporated it into a new 3D MPI-parallel Adaptive Mesh Refinement (3D-AMR) algorithm that I helped test and validate. I will be a coauthor an upcoming publication in preparation by Greenwood et (2017), which will feature my work on this 3D-AMR code.
- Did new simulations to show that the phase field equations with thermal fluctuations can be used to self-consistently simulate two-phase nucleation and growth for a robust range of alloy systems simply in terms of four physical parameters in the system: interface energies, liquid-state diffusion coefficient, free energy curvature of each phase near equilibrium, and nucleation barrier for solidification.
- Development of post-simulation analysis codes to study simulation results. A second paper that I will be primary author on will be written by expanding on the results presented at the end of the thesis later in 2017.

Acknowledgments

I would like to thank my supervisor Dr Nikolas Provatas for his patience, guidance, and insight, and most of all, taking a chance on me and guiding me through this very cool project. My thanks also goes to Tatu, Lei, and Sebastian, for their enjoyable company, putting up with my millions of (silly) questions, and also showing me the ropes. I would finally like to thank the ACSR group for our fun occasional outings and antics.

Introduction

In the past 2 decades or so, phase field models have seen an explosive growth in their use for exploring non-equilibrium phase transformations and microstructure evolution in materials science and engineering. Their connections with statistical thermodynamics makes them a fundamental reference form which to describe complex phase transformations once an appropriate set of order parameters and their symmetries are identified for a particular system. Dynamical equations of motions for such order parameter fields can be formulated based on free energy minimization principles and conservation laws. They are very simple to code and require little overhead in terms tracking moving, impinging and coalescing interfaces -the quintessential feature of non-equilibrium microstructure processes. Phase field models have been applied to a wide range of phenomena ranging from single-crystal solidification, directional and polycrystalline solidification, grain growth, elasticity and precipitation. These days they can also be used quantitatively for select phenomena in solidification and solid state transformations, making them viable tools for materials science and engineering. Quantitative calculations with phase field models requires detailed asymptotic boundary layer analysis, which prescribes how to match their bahaviour with appropriate sharp interface models in the limit when a suitable scale separation exists between the length of diffusion of impurities (or heat) and phase coexistence boundaries (hereafter called interfaces). The remainder of this section goes through a brief history of some of the major milestones in phase field modelling in recent years.

 $oldsymbol{1}$ Introduction

1.0.1 Single-order parameter phase field models

One of the first phase field models of solidification of a pure substance was by Kessler and Levine [5], which used the "model C" of the Hohenberg and Halperin classification [6] to demonstrate thermally-controlled solidification. Using matched asymptotic boundary layer analysis, Karma and Rappel [7] later showed how a phase field model of a pure material can quantitatively map onto the dynamics of the corresponding Stefan model (hereafter sharp-interface model) of solidification of a pure material [8] while operating with thin-rather than atomically sharp- order parameter interfaces. Specifically, it decoupled the time scale of phase field simulations from the atomic kinetics through the interface, a feature absent from so-called first order asymptotic mapping of the phase field model onto the sharp-interface approach derived by Caginalp [9]. At around the same time, Provatas et. al developed a novel dynamic adaptive mesh refinement algorithm [10, 11] for phase field models that dramatically reduced the computational barrier of grid discretization that makes data management and CPU times associated with large scale and long-time simulations of free boundary problems intractable.

In the scope of alloy materials, the work of Warren and Boettinger [12] later developed a specialized two-phase alloy model that demonstrated many of the qualitative features of casting could be modelled by coupling an order parameter to a solute concentration field, instead of a temperature field. Karma and co-workers [13, 14] adapted the thin-interface asymptotic analysis for a single-phase field model of solidification of an ideal binary alloy. Attaining the sharp interface limit for alloy solidification is made difficult by the large disparity in solute diffusion between the solid and liquid. Specifically, spurious solute trapping and lateral diffusion effects are generated through the interface. While physical in origin, these effects are negligible at low rates of solidification since the interface width is on the scale of nm. However, when employing diffuse interfaces for numerical expediency, these spurious kinetics become undesirably exaggerated. To remedy this, Refs. [13, 14] introduced a so-

called anti-trapping flux to correct for spurious solute trapping. They also employed select interpolation functions to interpolate the free energy between solid and liquid, which effectively transforms the driving force for solidification into the difference in grand potential between phases, leading to complete decoupling of solute and order parameter in equilibrium. This makes it possible to select the phase field interface width arbitrarily wide, and independently of the solute field. Ramirez et al. [15] later applied a thin interface analysis to the single-phase alloy model coupled to a thermal transport. Their results confirmed that the thin interface asymptotic analysis of Ref. [14] continue to hold for low cooling rates even for non-isothermal conditions.

Subsequent work by Tong et al. [4] adapted the thin interface asymptotic analysis of Ref. [14] for the case of single-phase solidification of general binary alloys under non-isothermal conditions. At the heart of this approach was the fitting the free energy of the liquid or any solid near equilibrium using the mathematical form of an ideal binary alloy, but with temperature-dependent coefficients. Of ori-Opoku et al [3] later generalized the interpolation functions used in Ref. [14] to interpolate the free energy between liquid and multiple crystal orientations, each represented by its own order parameter. For the case of ideal alloys, this approach is effectively a multi-order parameter variant of the model in Ref. [14]. By utilizing the approach of Tong et al [4] to fit the liquid or solid free energy close to their equilibrium concentrations, the model of Ref. [3] effectively provides a quantitative multi-order parameter phase field theory for simulating poly-crystalline solidification of non-ideal binary alloys.

1.0.2 Multi-order parameter phase field models

Modelling of multiple ordered phases with phase field models goes back to the original multiple-order parameter models models used by Khachaturyan [16] for the study of ordered precipitates and other solid state phase transformations. These models consider a phase field as physical order parameter that distinguish between ordered phases and a matrix phase. The interface free energy is defined through gradients in

 $oldsymbol{1}$ Introduction

the order parameters, and interactions between ordered phases through a polynomial expansion in their corresponding order parameters ¹. The multi-order parameter approach has been used by several groups to model grain growth in solid state systems [21, 22]. Multi-component alloys have also also been studied using the the multi-order parameter approach by adding a chemical free energy contribution that interpolates between phases through the variation of the order parameter fields [23, 24, 25]; alternatively, Moelans recently introduced a phase fraction weighting of the free energy, which is done through specialized interpolation functions defined solely in terms of the order parameters [26]. For practical control of interface energies, the equilibrium interface energy is decoupled from the solute fields by employing the so-called auxiliary concentration approach of Refs. [27, 28, 29] (more on this method below). An exception to this is the multi-order parameter solidification model developed by Ofori-Opoku et al [3], which, as mentioned above, uses vector-field variants of the interpolation functions in Ref. [14]. The multi-order parameter approach has been widely used to examine a variety of multi-phase solid state transformations and solidification in pure materials and multi-component alloys [30, 24, 25, 31, 32, 3].

1.0.3 Phase field models with an orientation order parameter

A related line of research for form modelling polycrystalline solidification involves the coupling an single order parameter to an orientational field. The first works in this direction go back to Morin and Grant [33], who created a multi-well free energy based on a complex order parameter that had minima at multiple orientations. While not rotationally invariant, it was a first steps toward assigning multiple angles needed to emulate polycrystalline orientations. A different approach was later developed by the works of Kobayashi and Warren [34, 35, 36] to include a rotationally invariant orientational field that is coupled to a scalar order parameter field. This approach allows an arbitrary number of orientations to be simulated. Orientational phase field

¹These resemble the form of complex amplitude equations that come out of coarse graining of *PFC* models [17, 18, 19, 20]

methods were first developed for pure materials and then extended to binary alloys by Granasy and co-workers [37]. Attempts have been made recently to self-consistently derive field theories that couple an orientational field to scalar order parameter field directly from complex amplitude equations derived from PFC models of pure materials [38]. Key open questions hoped to be addressed by such approaches are: (1) the self-consistent derivation of an analytic the free energy and (b) how such phase field theories couple to microscopic properties emerging from the two-point correlation function that enters PFC theories. When coupled with stochastic fluctuations, the orientational field approach offers one of the most physically consistent approaches for simulating nucleation in polycrystalline solidification. It is also quite practical as it allows a significant reduction on computational overhead to model multiple orientations. Multi-order parameter models (or multi-phase field models, discussed below) without adaptive mesh refinement can typically handle on the order of $\sim 5-10$ orientations and phases before they become computationally inefficient. Another benefit of the orientational field approach is that nucleation of multiple phases via noise is done simultaneously through the orientational fields, thus avoiding inconsistencies with nucleating multiple phases in the same location, as is the case in multi-phase field approaches. To our knowledge, there is presently no variant of these orientation-phase field models that deals with multiple phases in complex alloys.

1.0.4 Phase field models based on phase fraction fields

A fundamentally different avenue for modelling multiple phases in multi-component alloys is the so-called *multi-phase field models*, developed by Steinbach and collaborators [39, 40, 41, 42, 43, 44, 45], which is applicable to both solidification and solid state transformations. The phenomenology of these models assigns each phase a *phase-fraction* field ². The bulk free energy is interpolated across interfaces or

²This distinction between phase-fraction fields and order parameters is not practically important in the sharp interface limit of solidification, but is fundamentally important when connecting phase field models to order parameters arising from purely microscopic theories.

f 1 Introduction

n-junctions by a phase-fraction weighted superposition of each phase's free energy, each expressed in terms of auxiliary concentration fields (more on this below). Interactions between phases are implemented via so-called *double obstacle* potentials, or other specialized polynomial interaction terms in the phase fractions. Interface energy is modelled by various gradient operator forms acting on the phase fractions. Dynamics of the phase fractions are evolved using non-conserved dynamics subject to the constraint that the phase fractions sum to one, though the use of Lagrange multipliers ³. Decoupling of surface energies from the solute profile across interfaces is achieved, as with some multi-order parameter models, through the introduction of multiple *auxiliary* (i.e. fictitious) concentration fields, one assigned to each ordered phase [27, 28, 29].

1.0.5 Decoupling solute concentration from the order parameter through the interface

The auxiliary concentration field method referred to above is used by various phase-field models for decoupling solute and phase fields in equilibrium. This is a practical stratagem for controlling of the interface energies that affect microstructure morphology in alloy solidification. It was developed by Kim, Kim and Suzuki [28, 29] for a single-phase binary alloy and Tiaden and co-workers [27] for multi-phase alloys. We explain this decoupling approach here for the simple case of a single-phase binary alloy. The approach of Tiaden et. al [27] defines a phase fraction field for each phase (e.g. one for solid, one for liquid). Physical solute is then defined as a phase fraction-weighted superposition of fictitious (auxiliary) solute fields (one per phase). The bulk free energy of a system is expanded as a phase fraction-weighted sum of free energies, each expressed in terms of auxiliary concentrations. Ref. [28] follows a similar approach, except the classic interpolation between phases using using an order parameter between solid and liquid is retained. The time evolution of

³Using Lagrange multipliers in the dynamics can lead to unphysical spurious non-local adsorption effects, whereby unwanted phase fractions appear in triple-junctions.

the solid/lquid phase fractions (or single order parameter in [28]) follows the usual free energy minimization, constrained in the former case to sum to one through a Lagrange multiplier. Auxiliary concentration fields follow the usual mass conservation dynamics, constrained, however, by the condition that the chemical potentials defined for each auxiliary concentration are equal at each point in space. This effectively amounts to maintaining a driving force in the phase field equation everywhere equal to the local difference in local grand potential between the two phases [46]. This approach is numerically laborious but allows the equilibrium interface interface energy in the model to decouple from the solute profile through the interface, for any interface width. In effect, this methods trades the freedom afforded by the choice of interpolation functions used in classical phase field models for the use of auxiliary concentration fields, through which physical concentration are defined.

1.0.6 Dealing with spurious interface kinetics caused by numerically diffuse interfaces

Despite the important benefit of decoupling solute and order parameter fields, early multi-phase (i.e. phase-fraction) and multi-order parameter models were not immune from solute trapping and spurious interface kinetic effects, which are exacerbated with the use of diffuse phase field interfaces. This phenomenon can typically be neglected to lowest order in solid-state transformations, where the rate of interface motion and the disparity of diffusion between phases is small. However, failure to eliminate such kinetics effects during the early stages of solidification can lead to incorrect interface structure and impurity micro-segregation of the final solidified system. Most of the early models based on phase fractions or order parameters described above suffered from this deficiency as they only employed first order asymptotic interface analysis to match model parameters to the sharp interface limit [40]. An exception to this is the work of Folch and Plapp [47], which adapted the thin interface asymptotics of Ref. [14] to work with a phase-fraction model for binary-eutectic solidification

8 1 Introduction

that approximated the free energy of each phase with a simple quadratic function in concentration. Another exception was the multi-order parameter phase field model of Ofori-Opoku and co-workers [3] mentioned above, which used an anti-trapping currents for each order parameter) to quantitatively model sharp interface kinetics across any [diffuse] solid-liquid interface.

1.0.7 Deriving phase field models in the grand canonical ensemble

Plapp [1] recently introduced an elegant re-formulation of the traditional single-phase binary alloy phase field model starting from a grand potential energy (GP) rather than the usual Helmholtz free energy approach. In this work, the phase field retains its classic meaning as an order parameter. The driving force for its evolution during solidification becomes the grand potential difference between the solid and liquid. The evolution equation for the physical concentration (proportional to density) is replaced in favour of its conjugate field, the chemical potential, an intensive and natural variable of the grand potential ensemble. In this ensemble, the solute field is derivable from the grand potential; it turns out to be an interpolation of two "auxiliary" solute fields (one per phase), each derived from the grand potential function of that phase. As such, this approach naturally interprets the un-physical "auxiliary fields" introduced in Refs. [28, 29] in terms of a self-consistent classical field theory formulated from a chemical potential and physical order parameter field. In the limit of a constant diffusion coefficient, the mathematical description of single-phase binary alloy solidification maps identically onto a thermal solidification model of a pure material [8]. This makes it possible to re-cycle much of the asymptotic analysis machinery developed for a pure material [7] to parameterize the sharp interface limit of a simple single-phase binary alloy. Moreover, by evolving the chemical potential directly, phase field models formulated in the grand potential ensemble do not require the same computational cost of having to locally match chemical potentials defined by fictitious solute fields. Recently, Nestler and co-workers extended the grand potential phase field approach to multi-component and multiple phase solidification by employing a

a grand potential energy formulated in terms of phase fractions [48, 49].

1.0.8 Model developed in this thesis

This work will have two thrusts. The first will derive a model for general multicomponent and multi-phase solidification through a grand potential functional formulated in terms of physical order parameters fields to describe ordered phases. Such model does not yet exist in the literature and will extend the previous work of Orofi-Opoku and Provatas [3]. The second thrust is to derive a set of simple equations of motion for the solidifying system that are cast in terms of local order parameters and the local supersaturation fields of solute components; supersaturation is defined as the chemical potential difference of a component relative to an equilibrium reference chemical potential. An advantage of writing the evolution equations in this form is that it allows us to model both near and relatively far-from equilibrium solidification conditions in a robust range of complex alloy systems where the free energies can be approximated parabolically. More importantly, it makes it easily make contact with the sharp interface kinetics of the model by mapping into previously-developed quantitative asymptotic analysis theories in the literature. Other advantages of deriving a multi-order parameter phase field model that operates in the grand potential ensemble include: the use of specialized interpolation functions is no longer required as in previous works, the extension to multiple components becomes straightforward, and the fundamental interpretation of all fields remains physical.

Following the model derivation of the multi-order model for binary and multiple components (latter shown in the appendix), we examine some of the equilibrium properties of the model. We then benchmark its performance in predicting spacing selection in classic eutectic lamellar growth. Finally, we use stochastic noise to simulate homogeneous nucleation and multi-phase grain growth, demonstrating how to control and interpret primary/secondary solid nucleation as a function of the asymptotic convergence parameter of the model. 10 Introduction

1.1 Paradigm of Two-Phase Solidification

Solidification typically occurs when one phase nucleates and grows from a liquid. Much work has been done on this problem in relation to dendritic growth and directional solidification. Another, less well studied paradigm of solidification occurs when multiple phase nucleate out of a melt. The multi-order parameter model derived herein is designed specifically for multiple thermodynamic phases. However, to keep the thesis within pages limits, I will demonstrate the model derived herein on the case of binary two-phase eutectic structures. These are at the heart of multi component alloy solidification. Such intricate two-phase structures are important for a variety of material science applications such as bridge cables and high strength steels. Many binary alloy systems have a eutectic region of solidification and thus it is of interest to be able to accurately and efficiently model and study such structures.

Typically in a eutectic solidification process, two solid phases (usually denoted α,β) emerge from a liquid phase below the eutectic line of the phase diagram and is of some composition. These phases are characterized by different solute levels determined by the equilibrium phase diagram. The type of structures that form generally depend on process parameters such as alloy composition, alloy system, cooling rate, etc. One hallmark structure that has been well studied are periodic lamellar eutectics [50, 2, 51]. This occurs when the concentration of the liquid is near the eutectic concentration. For liquids higher or lower than the eutectic concentrations, called *hypo-eutectic* and *hyper-eutectic* alloys, solidification proceeds in a two-step process, where the high-temperature phase emerges first followed by a low temperature phase that fills the remaining liquid that did not solidify at high temperatures. Figure 1.1 shows an example of some eutectic microstructures, and and Fig. 1.2 a diagram to help better visualize eutectic structures in relation to the phase diagram. These figures are both taken from [51]

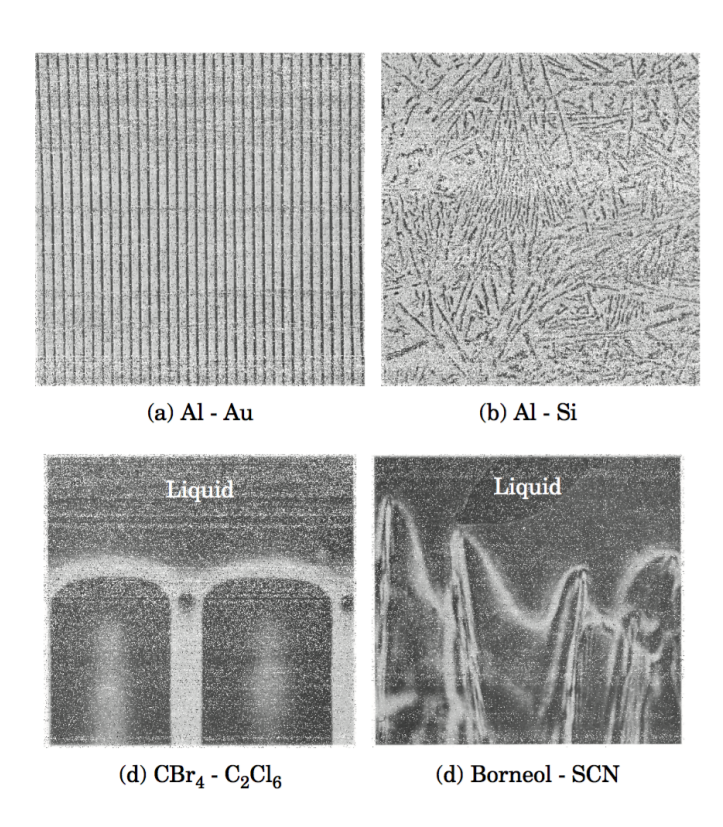


Figure 1.1: Experimental micrographs of regular and irregular eutectics: (a) regular Al-Au eutectic structure; (b) irregular Al-Si eutectic structure; (c) regular $CBr_4C_2Cl_6$; (d) irregular borneol-SCN eutectic

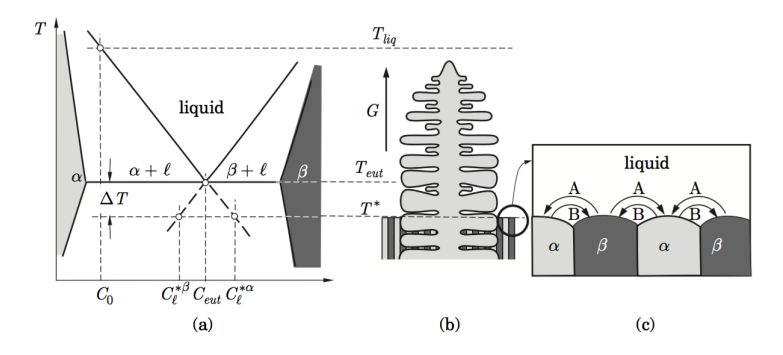


Figure 1.2: (a) Example eutectic phase diagram; (b) example eutectic microstructure form solidification; (c) a close up look at the lamellar structures showing coupled $\alpha - \beta$ growth

1 Introduction

1.2 Use of Adaptive Mesh Refinement in Phase Field modelling

As previously mentioned, phase field methods are robust for solidification, but desiring better quantitative treatments require more and more numerical and computational efficiencies. My Masters thesis work has been part of a collaboration to benchmark and improve a new 3D-MPI adaptive mesh refinement (AMR) code specifically designed for phase field simulations with my model equations. The code'e primary developer is Dr. Michael Greenwood, a former PhD student in the Provatas research group who is presently working at NR-Can. AMR was originally developed by Provatas et al [10] to increase the scalability for studying larger scale solidification processes by adapting meshes dynamically around moving fronts, which represent phase boundaries in microstructure evolution. My recent work to benchmark the this new AMR using the model derived in this thesis will be shown in an upcoming publication; however, the details of the new 3D AMR algorithm itself will not be shown in this thesis as that would greatly increase the length of this masters thesis and is beyond the scope of this study.

1.3 Outline of thesis

The remainder of this thesis is organized as follows:

• Chapter 2 (Sections 2.1-2.8) is dedicated to the derivation of a multi-order parameter model of solidification in the grand potential ensemble. We begin with a grand potential functional formulated in terms of multiple chemical potentials and phases. We derive the dynamical evolution equations for the order parameters and chemical potential fields, followed by an examination of the model's equilibrium properties. For quantitative applications, anti-trapping fluxes are added to the chemical potential equations in order to control the level of solute

1.3 Outline of thesis

trapping for diffuse interfaces. Thermal fluctuations are also incorporated into the theory and re-couched in dimensional form for each use. This "base" model serves as a platform for modelling multi-component and multi-phase solidification. The equations of motion of this base model are then specialized a multi-phase binary alloys whose free energies can be approximated by a 3-parameter quadratic form. This leads to an easy-to-use set of phase field equations that are shown to be a more general case of the well known phase binary alloy models that operate in the so called local supersaturation (near-to-equilibrium) limit of Ref. [1]. In the local supersaturation limit, model derived herein also effectively extends the model of Ref. [3] to multiple components.

• In Chapter 3 we benchmark our model and show some new results for two-phase nucleation. First we demonstrate that it reproduces the well-known results of Jackson and Hunt for predicting spacing of eutectic lamella. We also show the model reproduces other well-known features of eutectic growth such as lamellar instabilities during growth and "short circuit" diffusion between solid phases [51]. Following this, we examine the use of noise to simulate homogeneous nucleation to demonstrate two-phase nucleation in a Silver-Copper system. In particular we show how the use of different nucleation barriers affects the length scale and morphology of a two-phase grain growth. In quantitative phase field modelling it has become typical to use the nucleation barrier (denoted as $1/\lambda$) as a convergence parameter to control the interface width (denoted by W and given by $W \sim \lambda d_o$, where d_o is the capillary length of the material) and the diffusional time scale (denoted by τ and given by $\tau \sim \lambda W^2/D$, where D is the diffusion coefficient in the liquid); see [7, 13, 14, 46] for details. This is done for numerical convenience, to accelerate time and expand length scales in the numerical simulation of phase field models. This is possible because the capillary length of an interface (d_o) scales like the ratio $d_o \sim W/\lambda$. Here, we shown how λ can be used on the one hand as a numerical convergence parameter, but through appropriate scaling of time and length, we can still allow us to glean sensible

14 Introduction

results about certain metrics that depend on nucleation (controlled by λ). One such metric we focus on here is the solidified fraction versus time independent of λ in two-phase nucleation and growth simulations.

• The appendix contains the mathematical derivation that extend the the binary multi-component theory described in the text to multiple solute components and multiple phases. For interested readers, all the details of the mathematics of the derivation are worked in this appendix. In another section of the appendix, we discuss temperature incorporation into the model.

GRAND POTENTIAL PHASE FIELD MODEL

2.1 Grand Potential Thermodynamics

We start off with grand potential thermodynamics, contrary to the more traditional Helmholtz free energy typically used in PF modelling. In this ensemble, the temperature, volume and chemical potential are the dependent variable. It defined by

$$\Omega = F - \sum_{i} \mu_i N_i, \tag{2.1}$$

where F is the Helmholtz free energy, μ_i is the chemical potential of species i and N_i is the number of particles for the ith species. For each component, the chemical potential is defined by

$$\mu_i = \left. \frac{\partial F}{\partial N_i} \right|_{TV},\tag{2.2}$$

Equation (2.1) is a Legendre transformation on the Helmholtz free energy. As a result, it is straightforward to derive the well-known relation

$$d\Omega = -S dT - p dV - \sum_{i} N_i d\mu_i$$
 (2.3)

which implies that the natural variables of Ω are T, V and μ_i (whereas for the Helmholtz free energy they are S, V, N_i). Thus, by expressing Ω in terms of its

natural variables, we can immediately calculate the number of particles N as

$$N_i = -\frac{\partial \Omega}{\partial \mu_i} \bigg|_{T,V} \tag{2.4}$$

The description of alloys typically uses the composition as a measure of the amount of each species, instead of the number of particles of the species. We define compositions of the i^{th} species in terms of mole fractions as $c_i = N_i/N_A$, where N_A is Avogadro's number. Using this definition, we have

$$\Omega = F - \sum_{i} \frac{\partial F}{\partial N_{i}} N_{i}$$

$$= \nu_{m} f - \sum_{i} \frac{\nu_{m}}{N_{A}} \frac{\partial f}{\partial c_{i}} N_{A} c_{i}$$

$$= \nu_{m} \left(f - \sum_{i} \frac{\partial f}{\partial c_{i}} c_{i} \right)$$

$$\omega \equiv \frac{\Omega}{\nu_{m}} = f - \sum_{i} \mu_{i} c_{i},$$
(2.5)

where ν_m is the molar volume and where it is assumed implicitly that all phases have the same molar volume. Here ω is the grand potential density, while f is the Helmholtz free energy density. If there are n species in the system, there are only n-1 independent solute concentrations. To describe the system in terms of these n-1 independent concentration variables, we use mass conservation to write the n^{th} species as $c_n = 1 - \sum_{i}^{n-1} c_i$. Using this relation, the grand potential density is re-written as

$$\omega = \tilde{f} - \sum_{i}^{n-1} \mu_i c_i - \mu_n \left(1 - \sum_{i}^{n-1} c_i \right)$$

$$\omega + \mu_n = \tilde{f} - \sum_{i}^{n-1} (\mu_i - \mu_n) c_i$$

$$\tilde{\omega} = \tilde{f} - \sum_{i}^{n-1} \tilde{\mu}_i c_i,$$
(2.6)

where we have defined $\tilde{\omega} \equiv \omega + \mu_n c_n$ and $\tilde{\mu}_i \equiv \mu_i - \mu_n$, where $\tilde{\mu}$ is called simply the "chemical potential" of solute c_i hereafter. Similarly, \tilde{f} is the free energy of a phase in terms of the $c_1, c_2, \dots c_{n-1}$ independent concentrations. In these new variables, Eq. (2.2) becomes

$$\tilde{\mu}_i = \left. \frac{\partial \tilde{f}}{\partial c_i} \right|_{T,V} \tag{2.7}$$

while Eq. (2.4) becomes

$$c_i = -\left. \frac{\partial \tilde{\omega}}{\partial \tilde{\mu}_i} \right|_{T,V},\tag{2.8}$$

and in all cases the index i scans over each of the n-1 independent components. For simplicity of notation in what follows, we drop the tilde from $\tilde{\omega}$, \tilde{f} and $\tilde{\mu}$, as well as the $|_{T,V}$.

2.2 Grand Potential Phase Field Functional

This section constructs the grand potential phase field functional for multiple order parameters in the spirit of the approach developed by Ofori-Opoku et. al. [3]. To proceed, we first clarify some notion and introduce some variables. Let N denote the number of distinct ordered phases or orientations in the system. Define an order parameter vector, $\phi(\vec{r}) = (\phi_1(\vec{r}), \phi_2(\vec{r}), \cdots, \phi_N(\vec{r}))$, the components of which vary from

 $0 < \phi_i < 1 \ (i=1,2,3,\cdots N)$ and represent the order of one of N solid phases (or orientations) at any location in space. Through their interactions, order parameters will always satisfy $\phi_1 + \phi_2 + \cdots + \phi_N \leq 1$. For an n-component mixture, we define $\mu(\vec{r}) = (\mu_1(\vec{r}), \mu_2(\vec{r}), \cdots, \mu_{n-1}(\vec{r}))$ and $\mathbf{c}(\vec{r}) = (c_1(\vec{r}), c_2(\vec{r}), \cdots, c_{n-1}(\vec{r}))$, which are vector fields representing, respectively, n-1 chemical potentials and impurity concentration fields at any location in space. In what follows, we also define a set of interpolation functions denoted by $g_{\alpha}(\phi) \equiv g(\phi_{\alpha})$, whose specific form is specified later, but their limits must satisfy $g(\phi_{\alpha}) = 1$ when $\phi_{\alpha} = 1$ (the component α of $\phi(\vec{r})$ is one) and $g(\phi_{\alpha}) = 0$ when $\phi_{\alpha} = 0$ (all components α of $\phi(\vec{r})$ are zero).

In terms of these definitions, the following grand potential of a multi-phase and multi-component system is proposed,

$$\Omega[\boldsymbol{\phi}, \boldsymbol{\mu}] = \int_{V} \left\{ \omega_{\text{int}} \left(\boldsymbol{\phi}, \boldsymbol{\nabla} \boldsymbol{\phi} \right) + \sum_{\alpha=1}^{N} g_{\alpha}(\boldsymbol{\phi}) \omega^{\alpha}(\boldsymbol{\mu}) + \left[1 - \sum_{\alpha=1}^{N} g_{\alpha}(\boldsymbol{\phi}) \right] \omega^{\ell}(\boldsymbol{\mu}) \right\} d^{3}\boldsymbol{r} \quad (2.9)$$

In Eq. (2.9), the term $\omega_{\rm int}(\phi, \nabla \phi)$ tracks the free energy changes associated with solid-liquid interface and grain boundaries. The index α denotes and runs over solid phases, while l denotes the liquid. The function $\omega^{\vartheta}(\boldsymbol{\mu})$ ($\vartheta = \alpha$ or $\vartheta = l$) is the equilibrium grand potential density of phase ϑ written in terms of the n-1 non-equilibrium chemical potentials of the vector field $\boldsymbol{\mu}$. The functions $g_{\alpha}(\phi)$ thus interpolate the local grand potential density between phases via the order parameter components ϕ_{α} , each of which becomes one (and the others zero) in the bulk of the respective phases they represent.

Equation (2.9) assumes that each volume element is like a mini open system that is connected to a thermal heat bath with which it can exchange particles, and which does so subject to the local chemical potential μ . Consistent with density functional theories, thermodynamic equilibrium is attained when $\mu = \mu_{\rm eq}$, which is constant throughout the system and uniquely defines the equilibrium concentration field throughout the system.

2.2.1 Interaction between order parameters

The first term in Eq. (2.9) is ω_{int} is given by

$$\omega_{\text{int}}(\boldsymbol{\phi}, \boldsymbol{\nabla}\boldsymbol{\phi}) = \sum_{\alpha=1}^{N} \frac{\sigma_{\alpha}^{2}}{2} |\boldsymbol{\nabla}\phi_{\alpha}|^{2} + \sum_{\alpha=1} H_{\alpha} f_{\text{DW}}(\phi_{\alpha}) + \sum_{\alpha, \beta \neq \alpha} \omega_{\alpha\beta} \Psi(\phi_{\alpha}, \phi_{\beta})$$
(2.10)

where nominally σ_{α} are constants that set the solid-liquid interface energies, H_{α} defines the nucleation energy between solid α and liquid and $f_{\rm DW}$ is some double-well potential (with minima at $\phi_{\alpha}=0,1$). The term $\Psi(\phi_{\alpha},\phi_{\beta})\propto\phi_{\alpha}^2\phi_{\beta}^2+\cdots$ contains polynomial order interaction terms between different order parameters. In what follows, we retain only the second order pair-wise term, although other forms can also be added to all situations examined below. Following Refs. [22, 26], we can also make the σ_{α} more general functions of all the order parameters. In this case, all interface energies (solid-liquid and solid-solid) can be modelled by controlling σ_{α} , H_{α} and $\omega_{\alpha\beta}$. The interaction term strength $\omega_{\alpha\beta}$ assures that $\phi_1 + \phi_2 + \cdots \phi_N \leq 1$ everywhere in space. Loosely speaking, interactions such as these assure that no two ordered states overlap over the same point in space, save for grain boundaries. As such, the model above does not require that sum of all order parameters to strictly be 1. The actual value of $\phi_1 + \phi_2 + \cdots + \phi_N \leq 1$ in an equilibrated grain boundary depends on the type of grain boundary and its energy, which can be controlled through the polynomial interaction term strength and temperature as explored to an extent in [3].

2.2.2 Properties of the single-phase grand potential $\omega^{\vartheta}(\boldsymbol{\mu})$

The grand potential $\omega^{\vartheta}(\boldsymbol{\mu})$ of single phase ϑ (α, l) used in Eq. (2.9) is given by the Legendre transform of the free energy of the phase ϑ ,

$$\omega^{\vartheta}(\boldsymbol{\mu}) = f_{\vartheta}(c_1, \dots, c_{n-1}) - \sum_{i=1}^{n-1} \mu_i c_i,$$
 (2.11)

where f_{ϑ} is defined as the equilibrium Helmhotlz free energy function of phase ϑ and where the $\mu_i = \partial f_{\vartheta}/\partial c_i$ give the chemical potential of species i. Equation (2.11) assumes that f_{ϑ} is a convex function of the concentrations (important for special case discussed later), so that we can express the c_i as a unique function of the chemical potentials μ_i . The multi-component generalization of this is a mapping $\vec{\mu} \mapsto c_i(\vec{\mu})$ that maps the n-1 chemical potentials of the system into the same number of chemical potentials. Assuming such an invertible mapping exists, Eq. (2.11) can be written as

$$\omega^{\vartheta}(\boldsymbol{\mu}) = f_{\vartheta}(c_1(\mu_1, \dots, \mu_{n-1}), \dots, c_{n-1}(\mu_1, \dots, \mu_{n-1})) - \sum_{i=1}^{n-1} \mu_i c_i(\mu_1, \dots, \mu_{n-1}),$$
(2.12)

which then makes the grand potential a function of the chemical potentials, its natural variables. The analogue of Eq. (2.8) can be used to obtain concentration c_i in phase ϑ ,

$$c_i^{\vartheta} = -\frac{\partial \omega^{\vartheta}(\boldsymbol{\mu})}{\partial \mu_i} \tag{2.13}$$

In thermodynamic equilibrium, when μ^{eq} is substituted into Eq. (2.13), it yields the equilibrium concentrations c_i corresponding to phase ϑ , hereafter denoted by $c_i^{\vartheta(\text{eq})}$.

2.2.3 Concentration of a multi-phase system in the grand potential ensemble

Consider, next, the case of multi-phase system equilibrium described by the grand potential functional of Eq. (2.9). The *concentration field* of a species is now defined

everywhere by the functional generalization of Eq. (2.8) applied to Eq. (2.9), namely,

$$c_{i}(\boldsymbol{\phi}, \boldsymbol{\mu}) = -\frac{\delta\Omega}{\delta\mu_{i}}$$

$$= -\sum_{\alpha}^{N} g_{\alpha}(\boldsymbol{\phi}) \frac{\partial\omega^{\alpha}(\boldsymbol{\mu})}{\partial\mu_{i}} - \left[1 - \sum_{\alpha}^{N} g_{\alpha}(\boldsymbol{\phi})\right] \frac{\partial\omega^{\ell}(\boldsymbol{\mu})}{\partial\mu_{i}}$$

$$= \sum_{\alpha}^{N} g_{\alpha}(\boldsymbol{\phi}) c_{i}^{\alpha}(\boldsymbol{\mu}) + \left[1 - \sum_{\alpha}^{N} g_{\alpha}(\boldsymbol{\phi})\right] c_{i}^{\ell}(\boldsymbol{\mu}), \tag{2.14}$$

It is recalled that $\omega^{\vartheta}(\boldsymbol{\mu})$ is the equilibrium grand potential function of phase $\vartheta(=\alpha,l)$, evaluated at the field value $\boldsymbol{\mu}$. The concentration field $c_i(\boldsymbol{\phi},\boldsymbol{\mu})$ becomes $c_i^{\vartheta}(\boldsymbol{\mu})$ (i.e. Eq. (2.13)) within the bulk of each phase ϑ , and interpolated between corresponding values of $c_i^{\vartheta}(\boldsymbol{\mu})$ across interfaces by $\boldsymbol{\phi}$. The explicit variation of Ω from which $c_i(\boldsymbol{\phi},\boldsymbol{\mu})$ is derived is given by Eq. (2.17). It is noted that when $\boldsymbol{\mu} \to \boldsymbol{\mu}^{\text{eq}}$, Eq. (2.14) expresses an interpolated equilibrium concentration profile between coexisting solid-liquid phases, or solid-solid phases (depending on what equilibrium $\boldsymbol{\mu}^{\text{eq}}$ defines). The $c_i^{\vartheta}(\boldsymbol{\mu})$ in Eq. (2.14) shall hereafter be referred to as auxiliary fields [29].

The strategy of the grand potential formalism is as follows: the form of $\omega^{\vartheta}(\boldsymbol{\mu})$ in Eq. (2.12) is first found for all phases ϑ by inverting the system of chemical potentials (if possible) to find the phase concentrations $c_i^{\vartheta}(\boldsymbol{\mu})$. Once derived, the $\omega^{\vartheta}(\boldsymbol{\mu})$ are substituted into Eq. (2.9) to describe the local grand potential density of a multiphase, multi-component system in terms of chemical potential. The procedure leading to Eq. (2.12) is practical if the relations for $\mu_i(c)$ are invertible. For example, if $\mu_i(c)$ is non-convex, the mapping from μ_i to c_i^{ϑ} is not unique. Alternatively, if $\mu(c_i)$ depend on gradients of the concentration, as in the case of spinodal decomposition, it is also not possible to obtain an algebraic mapping. Numerical mappings is another story, and may be doable. But once again, it is entirely dependent on the system in question.

2.3 Phase Field Dynamics

In traditional phase field models, the dynamics of the fields ϕ_{α} are assumed to follow dissipative dynamics that relax a free energy while coupled to the evolution of conserved solute fields c_i . Here, we will employ a different approach where we couple the evolution of the order parameters ϕ_{α} to the evolution of the intensive variables μ_i that enter Ω , and which implicitly also govern the flow of c_i . This will prove to have several practical features.

2.3.1 Traditional form

Order parameters are non-conserved internal degrees of freedom in the system. As a result, the dynamics of each order parameter follows non-conserved gradient flow (what is known as *model A* dynamics),

$$\frac{\partial \phi_{\alpha}}{\partial t} = -M_{\phi_{\alpha}} \frac{\delta \Omega}{\delta \phi_{\alpha}} + \xi_{\phi}, \tag{2.15}$$

where $M_{\phi_{\alpha}}$ define a suitable time scale for the relaxation of ϕ_{α} . The stochastic variable ξ_{ϕ} accounts for thermal fluctuations and follows the standard fluctuation-dissipation theorem [52].

The evolution of each solute species follows mass conservation dynamics driven by a solute flux that formally coupes to the chemical potential of each species. This is given by conserved $(model\ B)$ dynamics,

$$\frac{\partial c_i}{\partial t} = -\nabla \cdot \boldsymbol{J}_{c_i} + \xi_c$$

$$= \nabla \cdot \left(\sum_{i=1}^{n-1} M_{ij}(\boldsymbol{\phi}, \boldsymbol{c}) \nabla \mu_j \right) + \nabla \cdot \vec{\zeta}.$$
(2.16)

Where the $M_{ij}(\boldsymbol{\phi}, \boldsymbol{c})$ are Osanger-type mobility coefficients for mass transport. Their form depends on the phase fields and concentrations. Their detailed forms for select

solid alloy phases has been worked out elsewhere [53]. The noise $\vec{\zeta}$ is a conserved noise flux governing fluctuations in concentration [52].

In what follows, we analyze the above equations of motion in the absence of noise, and return to the incorporation of thermal fluctuations in Section 2.8.

2.3.2 Reformulation of phase field model dynamics in terms of ϕ and μ

In the grand potential ensemble, it is the order parameters ϕ_i and chemical potentials μ_i that are evolved in time as these are the natural variables of the grand potential that change in space and time. This requires that Eq. (2.16) be re-written with the c_i expressed in terms of the set $\{\mu_i\}$. To proceed, the variation of Ω with respect to each respective field ϕ_{α} ($\alpha = 1, 2, \dots, N$) and μ_i ($i = 1, 2, \dots, n$) is required. This becomes

$$\delta\Omega = \int_{V} \left(\sum_{\alpha}^{N} \left\{ -\sigma_{\alpha}^{2} \nabla^{2} \phi_{\alpha} + H_{\alpha} f_{\mathrm{DW}}'(\boldsymbol{\phi}_{\alpha}) + \sum_{\beta \neq \alpha} 2 \,\omega_{\alpha\beta} \phi_{\alpha} \phi_{\beta}^{2} + g_{\alpha}'(\boldsymbol{\phi}) \left[\omega^{\alpha}(\boldsymbol{\mu}) - \omega^{\ell}(\boldsymbol{\mu}) \right] \right\} \delta\phi_{\alpha} + \sum_{i} \left\{ \sum_{\alpha}^{N} g_{\alpha}(\boldsymbol{\phi}) \frac{\partial \omega^{\alpha}(\boldsymbol{\mu})}{\partial \mu_{i}} + \left[1 - \sum_{\alpha}^{N} g_{\alpha}(\boldsymbol{\phi}) \right] \frac{\partial \omega^{\ell}(\boldsymbol{\mu})}{\partial \mu_{i}} \right\} \delta\mu_{i} \right) d^{3}\boldsymbol{r}.$$
(2.17)

where primes in Eq. (2.17) refers to differentiation with respect to the component ϕ_{α} of ϕ , and so $g'_{\alpha}(\phi) \equiv g'(\phi_{\alpha})$ throughout. Eq. (2.17) will be used as a generating functional for the equations of motion in what follows.

2.3.3 Order parameter equaitons

The variational of Eq. (2.17) with respect to the order parameters ϕ_{α} gives the evolution equation for each order parameter as

$$\frac{1}{M_{\phi_{\alpha}}} \frac{\partial \phi_{\alpha}}{\partial t} = \sigma_{\alpha}^{2} \nabla^{2} \phi_{\alpha} - H_{\alpha} f_{\text{DW}}'(\phi_{\alpha}) - \sum_{\beta \neq \alpha} 2\omega_{\alpha\beta} \phi_{\alpha} \phi_{\beta}^{2} - \left[\omega^{\alpha}(\boldsymbol{\mu}) - \omega^{\ell}(\boldsymbol{\mu})\right] g_{\alpha}'(\boldsymbol{\phi})$$
(2.18)

The square brackets on the right hand side of Eq. (2.18) define the thermodynamic driving force. At equilibrium, the chemical potentials μ_i ($i=1,2,\cdots n-1$) comprising the vector $\boldsymbol{\mu}$ become constant throughout the system (and the c_i^{ϑ} defined by Eq. (2.13) attain their equilibrium values in each phase). The equilibrium chemical potentials and concentrations are denoted, component-wise, by $\mu_i = \mu_i^{\text{eq}}$. It is also noted that at equilibrium (stable or metastable), solid and liuid phases satisfy $\omega^{\alpha}(\mu_1^{\text{eq}}, \cdots, \mu_{n-1}^{\text{eq}}) = \omega^l(\mu_1^{\text{eq}}, \cdots, \mu_{n-1}^{\text{eq}})$. Thus, at equilibrium, the driving force for the evolution of the ϕ_{α} goes to zero and the order parameters fields decouple from the chemical potential fields (or concentration fields) completely.

2.3.4 Chemical potential equations

Noting from Eq. (2.14) that c_i are functions of ϕ_{α} and μ_i the time derivative of c_i becomes

$$\frac{\partial c_i}{\partial t} = \left(\sum_{\alpha}^{N} \frac{\partial c_i}{\partial \phi_{\alpha}} \frac{\partial \phi_{\alpha}}{\partial t} + \sum_{j} \frac{\partial c_i}{\partial \mu_j} \frac{\partial \mu_j}{\partial t}\right)$$
(2.19)

Generalizing the susceptibility parameter introduced in Refs. [1], we define a generalized susceptibility matrix by

$$X_{ij} \equiv \chi_i(\boldsymbol{\phi}, \mu_j) \equiv \frac{\partial c_i}{\partial \mu_i} = \sum_{\alpha}^{N} g_{\alpha}(\boldsymbol{\phi}) \frac{\partial c_i^{\alpha}(\boldsymbol{\mu})}{\partial \mu_j} + \left[1 - \sum_{\alpha}^{N} g_{\alpha}(\boldsymbol{\phi}) \right] \frac{\partial c_i^{\ell}(\boldsymbol{\mu})}{\partial \mu_j}, \quad (2.20)$$

From Eq. (2.14) it is found that

$$\frac{\partial c_i}{\partial \phi_{\alpha}} = g'_{\alpha}(\boldsymbol{\phi}) \left[c_i^{\alpha}(\boldsymbol{\mu}) - c_i^{\ell}(\boldsymbol{\mu}) \right]$$
 (2.21)

Substituting Eqs. (2.20) and (2.21) into Eq. (2.19), the mass transport equations, Eq. (2.16), becomes (dropping the noise term),

$$\frac{\partial \mu_i}{\partial t} = \sum_{j}^{n-1} \left(X^{-1} \right)_{ij} \left[\nabla \cdot \left(\sum_{k}^{n-1} M_{jk}(\boldsymbol{\phi}, \boldsymbol{c}) \nabla \mu_k \right) - \sum_{\alpha} g_{\alpha}'(\boldsymbol{\phi}) \left[c_j^{\alpha}(\boldsymbol{\mu}) - c_j^{\ell}(\boldsymbol{\mu}) \right] \frac{\partial \phi_{\alpha}}{\partial t} \right]$$
(2.22)

where $(X^{-1})_{ij}$ denotes the (i,j) component of the inverse of the matrix X_{ij} .

Eqs. (2.18) and (2.22), along with the $c_i^{\alpha} = \partial \omega^{\alpha}(\boldsymbol{\mu})/\partial \mu_i$ and the definitions for $\omega^{\vartheta}(\boldsymbol{\mu}) = f_{\vartheta}\left(\left\{c_i^{\vartheta}\right\}\right) - \sum_{i=1}^{n-1} \mu_i c_i^{\vartheta}$ comprise a complete set of equations for N order parameters (ϕ_{α}) and n-1 chemical potential fields (μ_i) . For one component (i=1) and constant mobility, these equations map onto a phase field model for thermal solidification of a pure material (shown explicitly later).

2.4 Equilibrium Properties of Grand Potential Functional

One of the most important features of the so-called *quantitative* phase field models is that the equilibrium order parameter profiles decouple from concentration. This makes it possible to specify interface energy independently of the solute profiles through the interface, a practical feature for incorporating the results of microscopic studies of surface energy [54, 55, 19, 56]. This decoupling also eliminates the cap on the size of the diffuse interface that can be used, which is numerically expedient [14, 47, 3].

2.4.1 Equilibrium concentration field

The local concentration of each species in the multi-phase, multi-component system defined by Eq. (2.14). In a multi-phase equilibrium, the concentration field is given by

$$c_i^{\text{eq}}(\phi) = \sum_{\alpha}^{N} g_{\alpha}(\phi) c_i^{\alpha(\text{eq})} + \left[1 - \sum_{\alpha}^{N} g_{\alpha}(\phi) \right] c_i^{l(\text{eq})}, \tag{2.23}$$

where the $c_i^{\vartheta(\text{eq})} = c_i^{\vartheta}(\boldsymbol{\mu} = \boldsymbol{\mu}^{\text{eq}})$ denotes the bulk equilibrium concentration of phase ϑ (i.e., when $\mu_i = \mu_i^{\text{eq}} \ \forall i$). It is noted that the equilibrium concentration field c_i^{eq} is a function of space *only* through the order parameters, a manifestation of the decoupling of order parameters and solute fields at equilibrium in the grand potential formulation.

2.4.2 Equilibrium solid-liquid interfaces

To better appreciate how the above decoupling works, consider first solid-liquid coexistence along a planar 1D front. This involves a single phase α and the liquid. In equilibrium, all chemical potentials μ_i are everywhere constant throughout the system. As a result, the grand potential density functions of solid and liquid must be equal, i.e., $\omega^{\alpha}(\boldsymbol{\mu}^{\text{eq}}) = \omega^{\ell}(\boldsymbol{\mu}^{\text{eq}})$. Under these conditions, the Euler-Lagrange equation for the ϕ_{α} become

$$\sigma_{\alpha}^{2} \partial_{x}^{2} \phi_{\alpha} - H_{\alpha} f_{\text{DW}}'(\phi_{\alpha}) = 0, \tag{2.24}$$

For this case, the solid-liquid interface is determined entirely by the choice of σ_{α} , H_{α} and f_{DW} . For a simple ϕ -4 theory, Eq. (2.24) gives the usual hyperbolic tangent profile, and the usual surface energy calculated in many places [14, 46].

2.4.3 Equilibrium solid-solid interfaces

To illustrate solid-solid coexistence,. For simplicity, we consider coexistence between two solids, α and β , in a eutectic alloy. Assign each phase with its own order parameter ϕ_a and ϕ_{β} . Consider a temperature $T = T_{\rm e} - \Delta T$, where $T_{\rm e}$ is the eutectic temperature and $\Delta T = T_e - T$. Equilibrium phase coexistence requires that $\omega^{\alpha}(\boldsymbol{\mu}^{\rm eq}(T)) = \omega^{\beta}(\boldsymbol{\mu}^{\rm eq}(T))$, while at this temperature $\omega^{l}(\boldsymbol{\mu}^{\rm eq}(T))$ describes a metastable liquid. Expanding $\omega^{\alpha}(\boldsymbol{\mu}^{\rm eq}(T))$, $\omega^{\beta}(\boldsymbol{\mu}^{\rm eq}(T))$ and $\omega^{l}(\boldsymbol{\mu}^{\rm eq}(T))$ in a Taylor series around $T_{\rm e}$ in powers of ΔT gives

$$\omega^{\vartheta}(\boldsymbol{\mu}^{\mathrm{eq}}(T)) = \omega^{\vartheta}(\boldsymbol{\mu}^{\mathrm{eq}}(T_{\mathrm{e}})) - \sum_{i=1}^{n} \left(\left. \frac{\partial \omega^{\vartheta}}{\partial \mu_{i}} \right|_{\mu_{i}^{\mathrm{eq}}(T_{\mathrm{e}})} \left. \frac{\partial \mu_{i}^{\mathrm{eq}}}{\partial T} \right|_{T_{\mathrm{e}}} \right) \Delta T$$
 (2.25)

where $\vartheta = \alpha, \beta, l$. Using Eq. (2.13) in Eq. (2.25) and noting that $\omega^{\alpha}(\boldsymbol{\mu}^{eq}(T_e)) = \omega^{\beta}(\boldsymbol{\mu}^{eq}(T_e)) = \omega^{l}(\boldsymbol{\mu}^{eq}(T_e))$ gives,

$$\omega^{\alpha}(\boldsymbol{\mu}^{\text{eq}}(T)) - \omega^{l}(\boldsymbol{\mu}^{\text{eq}}(T)) = \sum_{i=1}^{n} \left\{ \left(\left. c_{i}^{\alpha(\text{eq})}(T_{\text{e}}) - c_{i}^{l(\text{eq})}(T_{\text{e}}) \right) \left. \frac{\partial \mu_{i}^{\text{eq}}}{\partial T} \right|_{T_{\text{e}}} \right\} \Delta T, \quad (2.26)$$

and a similar expression for the β phase. We define a new constant $\Gamma_s(T_{\rm e})$ by

$$\Gamma_s(T_e) \equiv \sum_{i=1}^n \left\{ \left(\left. c_i^{l(eq)}(T_e) - c_i^{s(eq)}(T_e) \right) \left. \frac{\partial \mu_i^{eq}}{\partial T} \right|_{T_e} \right\}, \quad s = \alpha, \beta$$
 (2.27)

The Euler-Lagrange equations for the steady state profiles $(\phi_{\alpha}^{o}, \phi_{\beta}^{o})$ for the α - β interface profiles become,

$$\sigma_{\alpha}^{2} \partial_{x}^{2} \phi_{\alpha}^{o} - H_{\alpha} f_{\text{DW}}^{\prime}(\phi_{\alpha}^{o}) - 2\omega_{\alpha\beta} \phi_{\alpha}^{o} \left(\phi_{\beta}^{o}\right)^{2} + \Gamma_{\alpha}(T_{\text{e}}) \Delta T g^{\prime}(\phi_{\alpha}^{o}) = 0$$

$$\sigma_{\beta}^{2} \partial_{x}^{2} \phi_{\beta}^{o} - H_{\beta} f_{\text{DW}}^{\prime}(\phi_{\beta}^{o}) - 2\omega_{\alpha\beta} \left(\phi_{\alpha}^{o}\right)^{2} \phi_{\beta}^{o} + \Gamma_{\beta}(T_{\text{e}}) \Delta T g^{\prime}(\phi_{\beta}^{o}) = 0, \tag{2.28}$$

Eqs. (2.28) is solved numerically, subject to the boundary conditions $\phi_{\alpha}^{o}(x \to -\infty) = 1$, $\phi_{\alpha}^{o}(x \to \infty) = 0$ for α , and $\phi_{\beta}^{o}(x \to -\infty) = 0$, $\phi_{\beta}^{o}(x \to \infty) = 1$ for β . It is noteworthy that the determination and are completely decoupled from the equilibrium

chemcial concentration fields $c_i^{\text{eq}}(x)$, and thus the interface energy of any two-phase combination can be predetermined numerically as a function of temperature. The temperature dependence in these equations allows control of the temperature dependence of grain boundary energy, a physical effect [57] that can in principle be controlled through the constants in Eqs. (2.28). As similar construction to the one shown here can be used to define two-phase boundary energies of other two-phase solid boundaries (e.g. polycrystalline or peritectics).

2.5 Non-Variational Dynamics for Diffuse Interfaces

For practical simulations of solidification it is crucial that phase field models reproduce the results of "accepted" sharp interface models of solidification in the limit when there is a clear separation of scales between the interface width (W) and the solute or thermal diffusion fields around a solidifying front. One way to do this in principle is to make the interface width small (denote this $W \ll d_o$, where d_o is the capillary length of the solid-liquid interface as shown by Caginalp [58, 59]). This is not practical however, as the grid resolution required would be difficult. Another severe issue with this limit is that it sets a microscopic small time scale for the phase field evolution, which makes numerical simulations at low undercooling impractical. The only hope for making phase field simulations involving solidification practical is to smear the interfaces of the ϕ_{α} fields. Doing so, however, creates spurious kinetics at the interface, excessive levels of solute trapping in bulk phases, and alters the flux conservation across interfaces from its classic form due to lateral diffusion and interface stretching. These effects are physically relevant at rapid rates of solidification where interface kinetics across the microscopic interface control solidification. For slow to moderate rates of solidification, however, these effects are negligible, and should be eliminated when using diffuse interface models to simulate solidification in real materials. The work of Refs. [60, 13, 14] has shown that these effects can be countered numerically by special choices of the interpolation function for solute diffusion and the chemical

potential, as well as the addition of a so-called *anti-trapping* flux in the mass transport equations. We adopt analogous tricks here.

The first modification referred to above is made by making the replacement $g_{\alpha}(\phi) \rightarrow h_{\alpha}(\phi)$ for the interpolation function in the concentration (Eq. (2.14)) and susceptibility (Eq. (2.20)). Namely, we modify the concentration field to

$$c_{i} = \sum_{\alpha}^{N} h_{\alpha}(\boldsymbol{\phi}) c_{i}^{\alpha}(\boldsymbol{\mu}) + \left[1 - \sum_{\alpha}^{N} h_{\alpha}(\boldsymbol{\phi})\right] c_{i}^{\ell}(\boldsymbol{\mu}), \tag{2.29}$$

from which the modified susceptibility matrix becomes

$$X_{ij} \equiv \chi_i(\boldsymbol{\phi}, \mu_j) = \sum_{\alpha}^{N} h_{\alpha}(\boldsymbol{\phi}) \frac{\partial c_i^{\alpha}(\boldsymbol{\mu})}{\partial \mu_j} + \left[1 - \sum_{\alpha}^{N} h_{\alpha}(\boldsymbol{\phi}) \right] \frac{\partial c_i^{\ell}(\boldsymbol{\mu})}{\partial \mu_j}, \tag{2.30}$$

where $h_{\alpha}(\phi) \equiv h(\phi_{\alpha})$ has the same boundary conditions as $g_{\alpha}(\phi)$ in bulk phases.

The second modification is to introduce an anti-trapping current

$$\boldsymbol{J}_{i}^{\mathrm{at}} = -\sum_{\alpha} a(\boldsymbol{\phi}) W_{\alpha} \left[c_{i}^{\ell}(\boldsymbol{\mu}) - c_{i}^{\alpha}(\boldsymbol{\mu}) \right] \frac{\partial \phi_{\alpha}}{\partial t} \frac{\boldsymbol{\nabla} \phi_{\alpha}}{|\boldsymbol{\nabla} \phi_{\alpha}|}, \tag{2.31}$$

where $a(\phi)$ is a function to be determined later through matched asymptotic analysis, W_{α} is the interface width, $\partial_t \phi_{\alpha}$ is the rate of the respective moving solid-liquid interface and $\hat{n}_{\alpha} = -\nabla \phi_{\alpha}/|\nabla \phi_{\alpha}|$ is the unit normal vector pointing into the liquid. The anti-trapping current modifies the mass conservation equation to

$$\frac{\partial c_i}{\partial t} = -\nabla \cdot \left(\boldsymbol{J}_{c_i} + \boldsymbol{J}_i^{\text{at}} \right), \tag{2.32}$$

Eqs. (2.29) and (2.32) thus modify Eq. (2.22) to

$$\frac{\partial \mu_{i}}{\partial t} = \sum_{j}^{n-1} \left(X^{-1} \right)_{ij} \left[\nabla \cdot \left(\sum_{k}^{n-1} M_{jk} \nabla \mu_{k} + \sum_{\alpha} a(\phi) W_{\alpha} \left[c_{j}^{\ell}(\boldsymbol{\mu}) - c_{j}^{\alpha}(\boldsymbol{\mu}) \right] \frac{\partial \phi_{\alpha}}{\partial t} \frac{\nabla \phi_{\alpha}}{|\nabla \phi_{\alpha}|} \right) - \sum_{\alpha} h_{\alpha}'(\phi) \left[c_{j}^{\alpha}(\boldsymbol{\mu}) - c_{j}^{\ell}(\boldsymbol{\mu}) \right] \frac{\partial \phi_{\alpha}}{\partial t} \right]$$
(2.33)

Following Ref. [26] we hereafter express the mobility matrix M_{jk} as

$$M_{jk} = \sum_{\alpha}^{N} q_{\alpha}(\boldsymbol{\phi}) D_{ji}^{\alpha} X_{ik}^{\alpha} + \left(1 - \sum_{\alpha}^{N} q_{\alpha}(\boldsymbol{\phi})\right) D_{ji}^{l} X_{ik}^{l}, \tag{2.34}$$

where D_{ij}^{ϑ} is the diffusion matrix of phase ϑ , and the repeated indices denote implied summation over the dummy index $i=1,2,\cdots n-1$. The function $q_{\alpha}(\phi)\equiv q(\phi_{\alpha})$ are any convenient interpolation functions introduced to vary between 0 in the liquid (all $\phi_{\alpha}=0$) and 1 in the solid (any $\phi_{\alpha}=1$) across any α grain. We have also defined two new matrices,

$$X_{ij}^{\alpha} \equiv \frac{\partial c_i^{\alpha}}{\partial \mu_j} = \frac{1}{\partial^2 f_{\alpha} / \partial c_i \partial c_j}$$

$$X_{ij}^l \equiv \frac{\partial c_i^l}{\partial \mu_j} = \frac{1}{\partial^2 f_l / \partial c_i \partial c_j},$$
(2.35)

Equation (2.33) describes multi-component diffusion, and is coupled, for multiphase solidification, to the order parameter equations Eq. (2.18), re-written here for convenience,

$$\tau_{\alpha} \frac{\partial \phi_{\alpha}}{\partial t} = W_{\alpha}^{2} \nabla^{2} \phi_{\alpha} - f'_{\text{DW}}(\phi_{\alpha}) - w_{obs} \phi_{\alpha} \sum_{\beta \neq \alpha}^{N} \phi_{\beta}^{2} - \hat{\lambda}_{\alpha} \left[\omega^{\alpha}(\boldsymbol{\mu}) - \omega^{\ell}(\boldsymbol{\mu}) \right] g'_{\alpha}(\boldsymbol{\phi}) \quad (2.36)$$

where $\hat{\lambda}_{\alpha} \equiv 1/H_{\alpha}$, $W_{\alpha} = \sigma/\sqrt{H_{\alpha}}$ and $\tau_{\alpha} \equiv 1/(M_{\phi}H_{\alpha})$. Also, to simplify matterrs, we will assume that the interaction term is a constant, i.e. $\omega_{\alpha\beta} = \omega_o$, for any ϕ_{α} and ϕ_{β} pair, and define a dimensionless interaction parameter, $\omega_{obs} = 2 \omega_o/H_{\alpha}$. We can in general define $\omega_{\alpha\beta}$ separately for any ϕ_{α} and ϕ_{β} to control the free energy of an

 α - β interface.

2.6 Multi-Phase Binary Alloy with Parabolic Free Energies

This section specializes Eqs. (2.33) and (2.36) to the case of a binary alloy (i = 1) of the case where the solid phases can be different, but whose free energies can be modelled by the quadratic form

$$f_{\vartheta} = \frac{A_{\vartheta}(T)}{2} \left(c - c_{\vartheta}^{min}(T) \right)^{2} + B_{\vartheta}(T), \quad \vartheta = \alpha, l, \tag{2.37}$$

close to some reference concentration. This functional form will provide us with a compact multi-phase binary model whose driving force is second order in supersaturation. This form makes it possible to fit a robust range of free energy curves of different phases through control of the coefficients A_{ϑ} , c_{ϑ}^{min} and B_{ϑ} , particularly if these are also made different on split intervals of concentration (or chemical potential) space. This is discussed again the end of this subsection.

2.6.1 Phase coexistence

It is instructive to begin by considering the equilibrium properties of a system of phases described by Eq. (2.37). Since we'll be concerned with multiphase solidification, we begin by considering liquid in coexistence with multiple solids. In terms of the above parabolic free energies, it is straightforward to seek a common tangent to describe coexistence between bulk liquid (concentration c_l^{eq}) and any bulk solid phase α (solid concentration c_{α}^{eq}), as well as the chemical potential μ_{α}^{eq} between these two

phases. These are found by solving

$$\frac{\partial f_l}{\partial c}\Big|_{c_l^{eq}} = \mu_{\alpha}^{eq}$$

$$\frac{\partial f_{\alpha}}{\partial c}\Big|_{c_{\alpha}^{eq}} = \mu_{\alpha}^{eq}$$

$$\frac{f_l - f_{\alpha}}{c_l^{eq} - c_{\alpha}^{eq}} = \mu_{\alpha}^{eq}$$
(2.38)

where

$$\mu = \frac{\partial f_{\vartheta}}{\partial c} = A_{\vartheta}(c - c_{\vartheta}^{min}), \quad \vartheta = \alpha, l$$
 (2.39)

is the chemical potential of each phase at concentration c. The solution of Eqs. (2.38) gives

$$c_{\vartheta}^{eq} = c_{\vartheta}^{min} + \frac{\mu_{\alpha}^{eq}}{A_{\vartheta}}, \quad \vartheta = l, s \tag{2.40}$$

where the equilibrium α -liquid chemical potential is

$$\mu_{\alpha}^{eq} = \frac{\Delta c_{\alpha}}{\chi^{l(eq)} \left(1 - k^{\alpha(\text{eff})}\right)} \left(\sqrt{1 + 2 \frac{\chi^{l(eq)} \left(1 - k^{\alpha(\text{eff})}\right)}{\Delta c_{\alpha}} \frac{\Delta B_{\alpha}}{\Delta c_{\alpha}}} - 1\right)$$
(2.41)

where the following definitions are used,

$$\Delta c_{\alpha} \equiv c_l^{min} - c_{\alpha}^{min}$$

$$\Delta B_{\alpha} \equiv B_l - B_{\alpha}$$

$$\chi^{l(eq)} \equiv 1/A_l$$

$$\chi^{\alpha(eq)} \equiv 1/A_{\alpha}$$

$$k^{\alpha(eff)} \equiv \chi^{\alpha(eq)}/\chi^{l(eq)}$$
(2.42)

The notation in Eq. (2.42) will be used in the steps below. The special limit where $A_l = A_{\alpha}$ is found by expanding the radical in Eq. (2.41) to leading order in $1 - k^{\alpha(\text{eff})}$,

yielding

$$\mu^{eq} = \frac{B_l - B_\alpha}{\left(c_l^{min} - c_\alpha^{min}\right)} \tag{2.43}$$

The parameters A_{ϑ} , c_{min}^{ϑ} and B_{ϑ} can then be used to fit the free energy of each phase and the phase diagram of the alloy.

2.6.2 Grand potential of a phase, and multi-phase concentration and susceptibility

The grand potential density of phase ϑ is expressed in terms of μ by eliminating the concentration using Eq. (2.39), namely,

$$\omega_{\vartheta} = f_{\vartheta}(c) - \mu c$$

$$= -\frac{\mu^2}{2A_{\vartheta}} - \mu c_{\vartheta}^{min} + B_{\vartheta}, \quad \vartheta = \alpha, l, \qquad (2.44)$$

From Eq. (2.44) the concentration of phase ϑ) is derived,

$$c_{\vartheta} = -\frac{\partial \omega_{\vartheta}}{\partial \mu} = \frac{\mu}{A_{\vartheta}} + c_{\vartheta}^{min}, \quad \vartheta = \alpha, l$$
 (2.45)

In a multi-phase system Eq. (2.45) is used to interpolate the local concentration via Eq. (2.29),

$$c(\boldsymbol{\phi}, \boldsymbol{\mu}) = \sum_{\alpha} h_{\alpha}(\boldsymbol{\phi}) c_{\alpha}(\boldsymbol{\mu}) + \left[1 - \sum_{\alpha} h_{\alpha}(\boldsymbol{\phi})\right] c_{l}(\boldsymbol{\mu})$$

$$= \sum_{\alpha} h_{\alpha}(\boldsymbol{\phi}) \left(\frac{\mu}{A_{\alpha}} + c_{\alpha}^{min}\right) + \left[1 - \sum_{\alpha} h_{\alpha}(\boldsymbol{\phi})\right] \left(\frac{\mu}{A_{l}} + c_{l}^{min}\right)$$

$$= \chi^{l(eq)} \left\{1 - \sum_{\alpha} \left(1 - k^{\alpha(eff)}\right) h_{\alpha}(\boldsymbol{\phi})\right\} \mu - \sum_{\alpha} \Delta c_{\alpha} h_{\alpha}(\boldsymbol{\phi}) + c_{l}^{min}, \quad (2.46)$$

The equilibrium concentration field between α and liquid is given by

$$c_{\alpha}^{\text{eq}}(\boldsymbol{\phi}) = \chi^{l(eq)} \left\{ 1 - \sum_{\alpha} \left(1 - k^{\alpha(\text{eff})} \right) h_{\alpha}(\boldsymbol{\phi}) \right\} \mu_{\alpha}^{\text{eq}} - \sum_{\alpha} \Delta c_{\alpha} h_{\alpha}(\boldsymbol{\phi}) + c_{l}^{min}, \quad (2.47)$$

Finally, from that last line of Eq. (2.46), the generalized susceptibility is derived via the prescription in Eq. (2.30),

$$\chi = \frac{\partial c}{\partial \mu} = \chi^{l(eq)} \left\{ 1 - \sum_{\alpha} \left(1 - k^{\alpha(\text{eff})} \right) h_{\alpha}(\boldsymbol{\phi}) \right\}, \tag{2.48}$$

It is clear that from Eq. (2.48) that the definition $\chi^{l(eq)} = \chi(\phi = 0)$ and $\chi^{\alpha(eq)} = \chi(\phi = \phi_{\alpha} = 1)$.

2.6.3 Casting the phase field equations in terms of supersaturation

From Eq. (2.39), it is found that

$$c^{l}(\mu) - c^{\alpha}(\mu) = \Delta c_{\alpha} + \chi^{l(\text{eq})} \left(1 - k^{\alpha(\text{eff})} \right) \mu \tag{2.49}$$

Meanwhile, from Eq. (2.40) we find

$$\Delta c_{\alpha} = \Delta c_{\alpha}^{\text{eq}} - \chi^{l(\text{eq})} \left(1 - k^{\alpha(\text{eff})} \right) \mu_{\alpha}^{\text{eq}}$$
 (2.50)

where $\Delta c_{\alpha}^{\rm eq}=c_{l}^{\rm eq}-c_{\alpha}^{\rm eq}$. Substituting Eq. (2.50) into Eq. (2.49), reduces Eq. (2.33) to

$$\chi(\boldsymbol{\phi}) \frac{\partial \mu}{\partial t} = \boldsymbol{\nabla} \cdot \left[D_L q(\boldsymbol{\phi}) \boldsymbol{\nabla} \mu + \sum_{\alpha} W_{\alpha} a(\boldsymbol{\phi}) \Delta c_{\alpha}^{\text{eq}} \left\{ 1 + \left(1 - k^{\alpha(\text{eff})} \right) U_{\alpha} \right\} \right. \frac{\partial \phi_{\alpha}}{\partial t} \frac{\boldsymbol{\nabla} \phi_{\alpha}}{|\boldsymbol{\nabla} \phi_{\alpha}|} \right] \\
+ \frac{1}{2} \sum_{\alpha} \Delta c_{\alpha}^{\text{eq}} \left\{ 1 + \left(1 - k^{\alpha(\text{eff})} \right) U_{\alpha} \right\} \frac{\partial \phi_{\alpha}}{\partial t}, \tag{2.51}$$

where we have introduced the supersaturation fields U_{α} , defined by

$$U_{\alpha} \equiv \frac{\chi^{l(\text{eq})}}{\Delta c_{\alpha}^{\text{eq}}} \left(\mu - \mu_{\alpha}^{\text{eq}} \right), \tag{2.52}$$

and where it can be shown that the mobility in Eq. (2.34) can be re-shaped into

$$q(\phi) \equiv \sum_{\alpha}^{N} q_{\alpha}(\phi) \frac{D^{\alpha}}{D_{L}} \chi^{\alpha(eq)} + \left(1 - \sum_{\alpha}^{N} q_{\alpha}(\phi)\right) \chi^{l(eq)} \to \tilde{q}(\phi) \chi(\phi), \tag{2.53}$$

where $\tilde{q}(\phi)$ has some general form that interpolates between 0 and 1 for $\phi = 1$ and $\phi = 0$, respectively. Using the second line of Eq. (2.44) to write $\omega^{\alpha}(\mu_{\alpha}^{eq}) - \omega^{l}(\mu_{\alpha}^{eq}) = 0$, gives

$$\Delta B_{\alpha} = \frac{\chi^{l(\text{eq})}}{2} \left(1 - k^{\alpha(\text{eff})} \right) \left(\mu_{\alpha}^{\text{eq}} \right)^2 + \Delta c_{\alpha} \mu_{\alpha}^{\text{eq}}$$
 (2.54)

Evaluating $\omega^{\alpha}(\mu) - \omega^{l}(\mu)$ using Eq. (2.44), and using Eq. (2.54), recasts the order parameter equations Eq. (2.36) as

$$\tau_{\alpha} \frac{\partial \phi_{\alpha}}{\partial t} = W_{\alpha}^{2} \nabla^{2} \phi_{\alpha} - f_{\text{DW}}'(\phi_{\alpha}) - w_{obs} \phi_{\alpha} \sum_{\beta \neq \alpha}^{N} \phi_{\beta}^{2} - \lambda_{\alpha} U_{\alpha} \left(1 + \frac{(1 - k^{\alpha(\text{eff})})}{2} U_{\alpha} \right) g_{\alpha}'(\phi)$$

$$(2.55)$$

where

$$\lambda_{\alpha} \equiv \frac{\hat{\lambda}_{\alpha} \left(\Delta c_{\alpha}^{\text{eq}}\right)^{2}}{\chi^{l(\text{eq})}} \tag{2.56}$$

In Eqs. (2.55), the definition $\hat{\lambda}_{\alpha} \equiv 1/H_{\alpha}$ and $\tau_{\alpha} \equiv 1/(M_{\phi_{\alpha}} H_{\alpha})$ continue to to hold.

2.7 Connection to Previous Models

This section shows how the general phase field model equations for multiple order parameters and chemical potential derived in the previous section, driven as it they are in terms of supersaturations, can trivially be mapped to other previous models in the literature by simply choosing different limits of its parameters.

2.7.1 Special case 1: Pure material solidification

It is worth noting that this accessible form of the model dynamics reduces exactly to the form describing solidification of a pure material. What is required is that one phase $(\phi_{\alpha} \to \phi)$ and thus dropping the interaction term, and to set the parabolic curvatures for solid and liquid $A_{\theta} = 1$. The order parameter dynamics become

$$\tau \frac{\partial \phi}{\partial t} = W^2 \nabla^2 \phi - f'_{\text{DW}}(\phi) - \lambda U g'(\phi)$$
 (2.57)

where $\lambda = 1/H$ is the inverse of the nucleation barrier of the single phase. Recasting the chemical potential in terms of $U_{\alpha} \to U$ and allowing constant diffusion in the solid and liquid phases (i.e. setting $q(\phi) = 1$) gives

$$\frac{\partial U}{\partial t} = \nabla \cdot (D\nabla U) + \frac{1}{2} \frac{\partial \phi}{\partial t}$$
 (2.58)

Of course we can drop the α subscripts at this point, and this is equivalent to the dynamics for the solidification of a pure material, similar as to what is studied in [7]

2.7.2 Special case 2: Polycrystalline dilute binary alloy solidification

We can also simplify the model in Eqs. (2.51) and (2.55) to the case of a single type of phase, with multiple solid grains (denoted by ϕ_{α} , $\alpha = 1, 2, 3, \cdots$) of a solidifying in a dilute binary alloy. In this case, one must take the *liquid* curvature to be 1, then select the solid phase curvature to any value such that $k^{\alpha(\text{eff})} \to k$, the equilibrium partition coefficient of a dilute binary alloy. Assuming, as do previous dilute alloy model in the literature, that we are weakly out of equilibrium, we can drop the second

order super saturation term, yielding

$$\tau \frac{\partial \phi_{\alpha}}{\partial t} = W^2 \nabla^2 \phi_{\alpha} - f'_{\text{DW}}(\phi_{\alpha}) - w_{obs} \phi_{\alpha} \sum_{\alpha t \neq \alpha}^{N} \phi_{\alpha t}^2 - \lambda U g'_{\alpha}(\phi)$$
 (2.59)

where α -specific components of U_{α} are the same for all α , and so the subscript is dropped and $U_{\alpha} \to U$. Recasting the chemical potential in terms of a single component supersaturation U gives

$$\left\{1 - (1 - k) \sum_{\alpha} h_{\alpha}(\phi)\right\} \frac{\partial U}{\partial t} = \nabla \cdot \left(D^{l} q(\phi) \nabla U\right)
+ \left\{1 + (1 - k) U\right\} \sum_{\alpha} W_{\alpha} a(\phi) \frac{\partial \phi_{\alpha}}{\partial t} \frac{\nabla \phi_{\alpha}}{|\nabla \phi_{\alpha}|} \right)
+ \left\{1 + (1 - k) U\right\} \sum_{\alpha} \frac{\partial h_{\alpha}(\phi_{\alpha})}{\partial t} \tag{2.60}$$

The form of the dynamics now is equivalent to that studied in [3]. By dropping the summands, we also recover the dynamics of the single crystal phase field model studied in Ref. [14].

2.7.3 Recovering the Supersaturation Limit of [1]

The remainder of this thesis works with order parameters that range from $-1 < \phi < 1$, and uses the following convenient interpolations,

$$g(\phi_{\alpha}) = \frac{15}{16} \left(\phi_{\alpha} - \frac{2\phi_{\alpha}^{3}}{3} + \frac{\phi_{\alpha}^{5}}{5} \right) + \frac{1}{2}$$

$$f_{DW}(\phi_{\alpha}) = -\frac{\phi_{\alpha}^{2}}{2} + \frac{\phi_{\alpha}^{4}}{4}$$

$$\sum_{\alpha} h(\phi_{\alpha}) = \sum_{\alpha} \frac{(\phi_{\alpha} + 1)}{2}$$

$$q(\phi) = \frac{(1 - \psi)}{2}, \quad \psi = N - \left\{ 1 - \sum_{\alpha} \phi_{\alpha} \right\}$$
(2.61)

In the case of a *single-phase* general binary alloy (with only a single order parameter $\phi_{\alpha} \to \phi$), the multi-order parameter model derived in the previous section reduces to Eqs. (2.59) and (2.60) with $k^{\alpha(\text{eff})} \to k^{\text{eff}}$. Thus is identical to the supersaturation limit of Ref. [1] (see Eqs. (110)-(110)). As such it has been shown to obey the following free-boundary problem

$$\frac{\partial U}{\partial t} = D_L \nabla^2 U \text{ (liquid)}$$

$$\left[1 + (1 - k^{\text{eff}})U_{\text{int}}\right] V_n = -D_L \frac{\partial U}{\partial n},$$

$$U_{\text{int}} = -d_o \kappa - \beta B V_n,$$
(2.62)

In terms of the concentration field, Eqs. (2.62) reduces to the well-know Stephan problem for solidification of a binary alloy,

$$\frac{\partial c}{\partial t} = D_L \nabla^2 c \text{ (liquid)}$$

$$c|_l (1 - k^{\text{eff}}) v_n = -D \frac{\partial c|_l}{\partial n},$$

$$c|_{\vartheta} = c_{\vartheta}^{eq} - \Delta c \left(d_o \kappa + \beta v_n \right), \quad \vartheta = s, l,$$
(2.63)

where d_o represents the capillary length and β the interface attachments kinetics coefficient. These coefficients are given in terms of the model parameters by the relationships

$$d_o = a_1 \frac{W}{\lambda}$$

$$\beta = a_1 \frac{\tau}{\lambda W} \left(1 - a_2 \lambda \frac{W^2}{\tau D} \right)$$

$$\lambda = \frac{15\Delta c^2}{16HX^{l(eq)}},$$
(2.64)

where the constants $a_1 = 0.8839$ and $a_2 = 0.6267$ for the choice of interpolations functions in Eq. (2.61). What we will hereafter refer to the classic sharp interface model will be the special case when $\beta = 0$, which occurs when $\bar{D} = D_L \tau / W_{\phi}^2 = a_2 \lambda$.

The supersaturation approach is almost exactly analogous to the original approach of [4], and leads to identical form of equations, except they used $k^{\text{eff}} \to c_s/c_l$. That is because the Tong et al effectively expand the grand potential using the functional form of the dilute alloy free energy, These sharp interface considerations lead us to our next section.

2.8 Thermal fluctuations in the phase field equations

To capture nucleation and interface fluctuations, phase field equations must introduce stochastic noise into each dynamical equation in order to emulate fast atomic-scale fluctuations that are washed out when one considers dynamical equations driven from a mean-field level free energy. In principle, this comes out formally from direct coarse graining using the methods of statistical mechanics [61]. However, when starting directly with PF models as mesoscale theories in their own right, noise must be added as stochastic noise in the equations of motion, effectively making them Langevin type equations [52]. This subsection studies how this is done for the phase field model defined by Eqs. (2.36) and (2.33).

We reproduce here the phase field equations of motion with stochastic noise fields added. For convenience, results are demonstrated for one order parameter and one solute field, and the anti-trapping term is discarded as it will not affect the results discussed in this sub-section. The order parameter and concentration equations become

$$\tau \frac{\partial \phi}{\partial t} = W_{\phi}^{2} \nabla^{2} \phi - f_{\text{DW}}'(\phi) - \hat{\lambda} \left[\omega^{\alpha}(\mu) - \omega^{\ell}(\mu) \right] g'(\phi) + \tau \xi, \tag{2.65}$$

$$\frac{\partial c_i}{\partial t} = \boldsymbol{\nabla} \cdot (M \boldsymbol{\nabla} \mu) - \nabla \cdot \vec{\zeta} \tag{2.66}$$

The previously defined constants are $\hat{\lambda} = 1/H$ and $\tau = 1/(M_{\phi}H)$, where M_{ϕ} is the mobility of the order parameter, M is the mobility of solute, and H is the nucleation barrier. The variable ξ is a stochastic scalar field and $\vec{\zeta}$ is a stochastic vector field.

Noise sources satisfy the fluctuation dissipation theorem [52, 62], namely

$$\langle \xi(\vec{x}, t)\xi(\vec{x}', t')\rangle = 2k_B T M_\phi \,\delta(\vec{x} - \vec{x}')\delta(t - t') \tag{2.67}$$

$$\langle \zeta_i(\vec{x}, t)\zeta_j(\vec{x}', t')\rangle = 2k_B T M \delta(\vec{x} - \vec{x}')\delta(t - t')\delta_{ij}$$
(2.68)

where ζ_i is the i^{th} component of $\vec{\zeta}$, and δ_{ij} is the Kronecker delta.

2.8.1 Non-dimensional form of the phase field equations

It will be useful to work in dimensionless time and space variables. We thus recast the above phase field equations and fluctuation dissipation relations in terms of dimensionless time ($\bar{t} = t/\tau$) and space ($\bar{x} = x/W_{\phi}$). With this rescaling, Eqs. (2.65) and (2.66) become

$$\frac{\partial \phi}{\partial \bar{t}} = \nabla^2 \phi - f'_{DW}(\phi) - \hat{\lambda} \left[\omega^{\alpha}(\mu) - \omega^{\ell}(\mu) \right] g'(\phi) + \eta, \tag{2.69}$$

$$\frac{\partial c_i}{\partial \bar{t}} = \boldsymbol{\nabla} \cdot \left(\bar{M} \boldsymbol{\nabla} \mu \right) - \nabla \cdot \vec{q}, \tag{2.70}$$

where the gradients are assumed in terms of \bar{x} , and where $\eta = \tau \xi$, $\vec{q} = (\tau/W_{\phi})\vec{\zeta}$, and $\bar{M} \equiv M\tau/W_{\phi}^2$. Applying these rescaling to the noise relations in Eqs. (2.67) and (2.68) yields their corresponding dimensionless counterparts,

$$\langle \eta(\vec{x}, \bar{t}) \eta(\vec{x}', \bar{t}') \rangle = 2 \frac{k_B T}{H W_{\phi}^d} \delta(\vec{x} - \vec{x}') \delta(\bar{t} - \bar{t}')$$
(2.71)

$$\langle q_i(\vec{x}, \bar{t}) q_j(\vec{x}', \bar{t}') \rangle = 2 \frac{k_B T}{W_\phi^d} \left(\frac{M\tau}{W_\phi^2} \right) \delta(\vec{x} - \vec{x}') \delta(\bar{t} - \bar{t}') \delta_{ij}, \tag{2.72}$$

To arrive at Eqs. (2.71) and (2.72) the delta functions were rescaled according to $\delta(\vec{x} - \vec{x}') \to \delta(\vec{x} - \vec{x}')/W_{\phi}^d$ and $\delta(t - t') \to \delta(\bar{t} - \bar{t}')/\tau$, where d is the dimension of space.

2.8.2 Simplification of the noise amplitude for the order parameter equation

To proceed, we first use $RT/\Omega_o = k_B T \bar{\rho}$, where Ω_o is the molar volume of the alloy (units of m^3/mole , and assumed to be the same in both phases) and $\bar{\rho}$ is its atomic density (units $\#/m^3$). This is used to re-write Eq. (2.71) as

$$\langle \eta(\vec{x}, t) \eta(\vec{x}', t') \rangle = 2 \left[\frac{RT}{\Omega_o H} \right] \frac{1}{W_\phi^d \bar{\rho}} \delta(\vec{x} - \vec{x}') \delta(\bar{t} - \bar{t}'), \tag{2.73}$$

The expression in the square brackets has a special significance, it is related to the dimensional constant, found in the preceding section:

$$\lambda = \frac{15\Delta c_{eq}^2}{16v_e^{eq}H},\tag{2.74}$$

where χ_l^{eq} is the inverse liquid free energy curvature with respect to concentration, and in general is in units of RT/Ω_o . We assume a diagonal susceptiblity and drop the indices in χ . Equation (2.74) changes to Eq. (2.64) for a general alloy at low supersaturation, whose form derived from Eqs. (2.33) and (2.36). It is intuitive to recast the form of the noise correlations in Eqs. (2.71) in terms of λ , which represents the inverse nucleation barrier, which also scales the thickness of the phase field interface [13, 14, 46]. Using the first of Eq. (2.64) to eliminate W_{ϕ} in terms of d_o transforms, using $\Delta c_{eq}^2/\bar{\chi}_l^{eq}$ (where $\bar{\chi}_l^{eq}$ is a dimensionless inverse liquid free energy curvature) and substituting in $\bar{\rho} = N_A/\Omega_o$ into Eq. (2.73) gives

$$\langle \eta(\vec{x}, t) \eta(\vec{x}', t') \rangle = 2(J \, a_1^d) \left[\frac{F_{\text{exp}}}{\lambda^{d-1}} \right] \delta(\vec{x} - \vec{x}') \delta(\bar{t} - \bar{t}')$$
 (2.75)

where J=16/15 and the dimensionless number $F_{\rm exp}$ is

$$F_{\rm exp} = \frac{\Omega_o \,\bar{\chi}_l^{eq}}{N_A \,\Delta c_{eq}^2 d_o^d} \tag{2.76}$$

The constants in Eq. (2.76) are extractable material experimental parameters. A similar approach is applicable to the solute equation [63, 64]. However that is not explored in this thesis. This work focuses on nucleation of phases. The order parameter dynamics for nuclei formation happen on a time and length scales much shorter and smaller than the diffusion processes. The numerical amplitude of the solute noise is significantly lower than the strength of the order parameter noise on these length and time scales [63, 64].

2.8.3 Calculation of the capillary length

The capillary length, d_o , is an important physical quantity defining the physical length scale of a material. Matched asymptotic boundary later analysis can be used to show that physical quantity is mapped onto the phase field parameter according to the relatioship $\lambda = a_1 W_{\phi}/d_o$ [46]. This is beyond the scope of this thesis. This is done by mapping the phase field equations onto their corresponding sharp interface model SIM. This model assumes that solidification is described by solute diffusion in the bulk phases in tandem with flux conservation across moving interfaces and the Gibbs Thomson condition controlling temperature or concentration value on either side of a "sharp" interface. The derivation of the sharp interface model will not be derived here. I quote here an expression from [65] where when one considers the sharp-interface model of single phase solidification (from liquid to solid), the Gibbs-Thomson condition is given in general by

$$c_{L,s} - c_{L,s}^{\text{eq}} = \frac{-2\sigma\Omega_o}{\Delta c_{eq}\Lambda^{\pm}} \kappa \tag{2.77}$$

where $c_{L,s}$ is the concentration in liquid or solid side of the interface, and $c_{L,s}^{\rm eq}$ are its corresponding equilibrium values. In 2.77, σ is the surface energy (which we can equivalently take to be γ , the surface tension, for a liquid), Ω_o the molar volume, Λ^{\pm} the inverse molar free energy curvature at equilibrium solid (+) or liquid (-), and κ is the interface curvature. Dividing both sides by Δc_{eq} and isolating the factor

multiplying κ , (and assuming a metric free energy density rather than a molar free energy) gives the capillary length on the liquid side of the interface as

$$d_o = \frac{2L_f\Gamma}{\Delta c_{eq}^2 T_m} \left(\frac{\partial^2 f}{\partial c^2}\right)^{-1},\tag{2.78}$$

where Γ is the Gibbs-Thomson coefficient, L_f the latent of fusion, and T_m the melting temperature, these three terms come from rearranging $\Gamma = \frac{\gamma T_m}{L_f}$. This derivation of the capillary length only requires knowledge of the curvature from the free energy curve. This is attractive for the parabolic free-energy phase field model derived in this section, since free energy curvature are precisely what goes into the model and are readily available. In this thesis, we assume that Γ is the same for both phases in a eutectic phase diagram, which is reasonable as in practice they are usually in the same order of magnitude.

2.9 Interpreting the role of λ in phase field modelling

As noted earlier, the λ , the inverse of the nucleation barrier, plays an important role in quantitative phase field modelling in the literature. To understand the role of λ , we consider in this section a simple case of a 1D interface evolving under generic *Model* C [6] dynamics for a pure material, described by

$$\tau_{\phi} \frac{\partial \phi}{\partial t} = W_{\phi}^{2} \frac{\partial^{2} \phi}{\partial x^{2}} - g'(\phi) - \lambda \Delta \bar{T} \theta P'(\phi)$$

$$\frac{\partial \theta}{\partial t} = D \frac{\partial^{2} \theta}{\partial x^{2}} - \frac{\partial \phi}{\partial t}$$
(2.79)

where ϕ is the order parameter, θ is a reduced diffusion field (temperature difference from the melting temperature), D a diffusion coefficient, $\Delta \bar{T}$ represents a dimensionless undercooling of the liquid and λ a coupling constant. While this situation describes solidification of a pure material, the discussion below is also valid for more complex alloys in general.

Consider next a steady state interface moving with some velocity V. We assume that the fields can be described in this case as $\phi(x,t) = \phi(x-Vt)$ and $\theta(x,t) = \theta(x-Vt)$. We can express the phase field time scale τ_{ϕ} and interface width W_{ϕ} in terms of the material parameters of the SIM via the asymptotically derived relationships of the form in Eq. (2.64), i.e. $d_o = a_1 W_{\phi}/\lambda$, $\beta = a_1 \tau_{\phi}/(W_{\phi}\lambda) \left\{1 - a_2 \lambda/\bar{D}\right\}$, where $\bar{D} = D\tau_{\phi}/W_{\phi}^2$. In the classic SIM, $\beta = 0$, and these relations give

$$\tau_{\phi} = (a_2/a_1^2) d_o^2 \lambda^3 / D$$

$$W_{\phi} = d_o \lambda / a_1 \tag{2.80}$$

Substituting Eqs. (2.80) into Eqs. (2.79) after changing variables to co-moving coordinates transforms Eqs. (2.79) to

$$\left(\frac{d_o^2 \lambda^2}{a_1^2}\right) \frac{\partial^2 \phi}{\partial \eta^2} + \left(\frac{a_2 d_o^2 V}{a_1 D} \lambda^3\right) \frac{d\phi}{d\eta} - g'(\phi) - \lambda \Delta \bar{T} \theta P'(\phi) = 0$$

$$D \frac{\partial^2 \theta}{\partial \eta^2} + V \frac{d\theta}{d\eta} + V \frac{d\phi}{d\eta} = 0$$
(2.81)

where $\eta = x - Vt$, and we used $\partial_x \to \partial_\eta$ and $\partial_t \to -V\partial_\eta$. It is clear that the selected speed V of the front (or local part of a front, such as a fat dendritic tip) described by Eq. (2.81) must be a function of the form $V = f_{PF}(d_o, D, \Delta \bar{T}, \lambda)$.

It is known from the microscopic theory of solvability (ms) [66, 67, 68, 69, 70, 71, 72], an analytical theory that solves the classic SIM to predict the growth rate of thermal dendrites, that the dendritic tip speed obeys $V_{\rm ms} = (D/d_o) f_{\rm ms}(\Delta \bar{T})$. Thus $V_c = D/d_o$ provides a natural characteristic solidification speed. Also, $l_c = d_o$ and $t_c = d_o^2/D$ provide, respectively, a characteristic length and time for the solidification. These are thus also natural variables with which to scale the phase field equations, which also obey SIM kinetics. Scaling space and time in Eqs. (2.81) by $y = \eta/d_o$ and

 $\bar{t} = t/(d^2/D)$ gives

$$\left(\frac{\lambda^2}{a_1^2}\right)\frac{\partial^2\phi}{\partial y^2} + \left(\frac{a_2\,\lambda^3}{a_1^2}\right)\bar{V}\frac{d\phi}{dy} - g'(\phi) - \lambda\Delta\bar{T}\,\theta\,P'(\phi) = 0$$

$$\frac{\partial^2\theta}{\partial y^2} + \bar{V}\frac{d\theta}{dy} + \bar{V}\frac{d\phi}{dx} = 0$$
(2.82)

where $\bar{V}=(d_o/D)V$. By inspection of Eq. (2.82), the scaled velocity \bar{V} can only depend on λ and $\Delta \bar{T}$, i.e. be a function of the form $\bar{V}=\bar{f}_{PF}(\Delta \bar{T},\lambda)$. Thus, the dimensional phase field velocity must be of the form $V=(D/d_o)\bar{f}_{PF}(\Delta \bar{T},\lambda)$.

It is clear that for the phase field and microscopic solvability (ms) theories to be compared, the phase field velocity V must be scaled in some way by λ . This makes sense since λ relates to the nucleation barrier, a degree of freedom that does *not* enter the SIM. Guidance on how to scale out λ is found by considering the characteristic speed implied by Eqs. (2.80), i.e.,

$$V_c^{\rm PF} = W_{\phi}/\tau_{\phi} = \left(\frac{D}{d_o}\right) \frac{a_1}{a_2} \frac{1}{\lambda^2}$$
 (2.83)

Equation (2.83) suggest that to make the PF and sharp interface model results agree (in this case depend only on $\Delta \bar{T}$), we should divide phase field results by λ^2 , which is what is done in quantitative demonstrations of PF modelling [7, 14, 46].

2.9.1 Interpreting the dual role of λ in the noise amplitude

As discussed above, the inverse nucleation energy, λ (inverse of a nucleation barrier) does not enter the sharp interface model of solidification. It must thus be scaled out of phase field results when comparing them to predictions of the SIM that depend on driving force. As a result, λ is often treated as a "free" parameter in PF modelling, typically chosen to smear the scale of the interface, such that λ -scaled PF results converge onto corresponding SIM results. However, it is recalled from Section 2.8 that λ also works its way into the amplitude of stochastic noise correlations in Eq. (2.75)

The choice of λ must thus be consistent in its two roles.

In the order parameter noise, Equation (2.75) shows that noise strength of the order parameter field (and temperature) decreases as λ increase. This makes sense since increasing λ is the same as increasing W_{ϕ} . As a result, the noise strength in the "coarse grained" volume, defined by expanding W_{ϕ} , must must decrease to maintain the noise strength the smaller physical volume d_o^d independent of W_{ϕ} .

Theses results also imply that when using PF noise in the diffuse interface limit, fluctuations will only be relevant on length scales larger than W_{ϕ} and time scales larger than τ_{ϕ} , which typically scaled to meso-scale values when $\lambda > 1$ is used. Conversely, that implies that fluctuations will be non-physical on length and time scales smaller than W_{ϕ} and τ_{ϕ} . A plausible fix to this problem may be to reduce λ during the nucleation phase of a simulation, and then increasing λ again later on in the simulation when the driving force for nucleation has significantly decreased due to solute segregation. Unfortunately, this will require an intractable number of numerical time steps until nucleation actually occurs, since decreasing λ also reduces the time scale of each numerical time step.

An alternate route is to scale up λ to values somewhat greater than one. In that case, the PF "nuclei" that emerge represent, very loosely speaking, a collection of nucleated solid that has emerged within a volume W_{ϕ}^d , and over the time scale τ_{ϕ} . If the actual time and length scales over which microstructure evolves is much larger than W_{ϕ} and τ_{ϕ} , respectively, this should not pose a problem to the interpretation of results seeded by nucleation and growth in the presence of diffuse-interfaces. This will be explored in the last part of the thesis.

RESULTS

This section first benchmarks the multi-order parameter phase field model in Eqs. (2.51) and (2.55) against some standard benchmark results for two-phase eutectic growth in binary alloys, for which theoretical predictions of the lamellar spacing is known. It then discusses the use of the model in examining the properties of two-phase homogenous nucleation. It begins by showing how one can relatively easily map the parameters of the model's parabolic free energies onto practical alloy system by matching the model's equilibrium properties to a desired phase diagram of a eutectic binary alloy. All simulations were carried out using a standard finite-difference Euler time-stepping algorithm, as described in [46, 3] (and many other papers and books), and is implemented in the previously mentioned AMR code.

3.1 Phase Diagram and Free Energy Construction

3.1.1 Ideal binary eutectic alloy

In this thesis, two alloy systems, with two types of phase diagrams, are used for some of the simulations shown. The first is an arbitrarily ideal symmetric binary mixture phase diagram shown in Fig. 3.1. An equilibrium phase diagram such as this is made by carrying our a *common tangent construction* ¹ between free energies of any two phases, at a given temperature. Three phase free energies are shown for

¹This is exactly the same as the Maxwell equal area construction.

48 3 Results

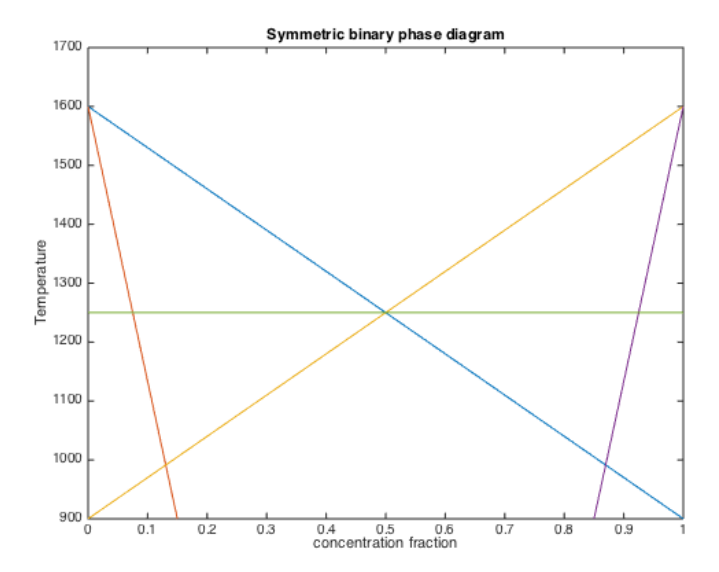


Figure 3.1: Ideal symmetric phase diagram for a fictitious alloy. Horizontal axis is concentration of solute and on the vertical axis is the temperature. Regions below the orange and purple lines are single phase coexistence of two solids (α to the left and β to the right. Regions above the blue and yellow lines corresponds to liquid phase. The region between the orange and blue denoted coexistence between one α solid and the liquid and the region between the purple and yellow denote coexistence between β solid and the liquid.

a specific temperature in Fig. 3.2. The phase diagram in Fig. 3.1 was constructed by selecting a $T_m = 1600K$, liquidus slope of 700 K/wt. frac. and an equilibrium partition coefficient of 0.15. The eutectic concentration is evident by the horizontal line occurring at T = 1250. For this fictitious alloy, we can fit the coefficients of the parabolic free energies at some temperatures by simply using the equilibrium conditions provided in section 2.6. This procedure is greatly simplified by assuming equal free energy curvatures (in this case, all were taken to be 1), and fixing the well height of the liquid phase such that only the well heights of the solid $\alpha\beta$ phases move with temperature. An example of what the free energies of the α , β and liquid phases look like at some temperature (above the eutectic) is given in Fig 3.2

3.1.2 Silver-copper alloy system

A more complex phase diagram comes from an approximate experimental free energy for eutectic Ag-Cu. The expressions for the solid and liquid free energies are taken

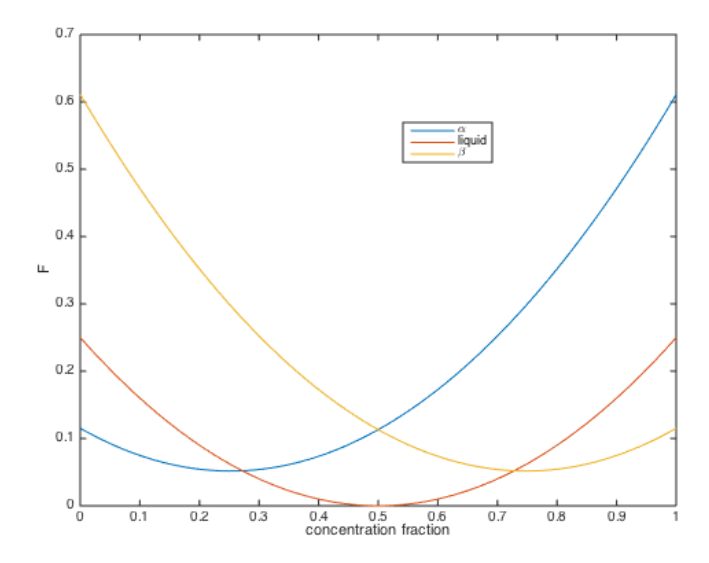


Figure 3.2: Parabolic free energies for fictitious alloy phases, at a specific temperature. Blue is α solid, yellow is β solid and orange is liquid. A simultaneously common tangent line to the blue and orange curves marks the concentrations of α solid (tangent to blue curve) and liquid (tangent to orange curve. A simultaneously common tangent line to the yellow and orange curves marks the concentrations of the β solid (tangent to yellow curve) and liquid (tangent to orange curve.

directly from [46]. Fig 3.3 shows the constructed phase diagram, the same book by Provatas and Elder [46]. The expressions for the free energies are not quoted here as they are quite long, and won't be used directly here. Readers interested in the full expression may refer to chapter 6 of the referenced book. The remainder of this subsection briefly describes the procedure in extracting parabolic free energies from such experimental free energies, that may come from a thermodynamic data base i.e. such as CALPHAD.

In principle, there a number of ways one can parabolically fit their system. We use a simple taylor series expansion to second order around the equilibrium composition (as found by a common tangent construction), and rearrange the resulting taylor series into the appropriate form as required for section 2.6. For example, consider an arbitrary solid free energy for an solid phase α (here, Greek letters denote solid

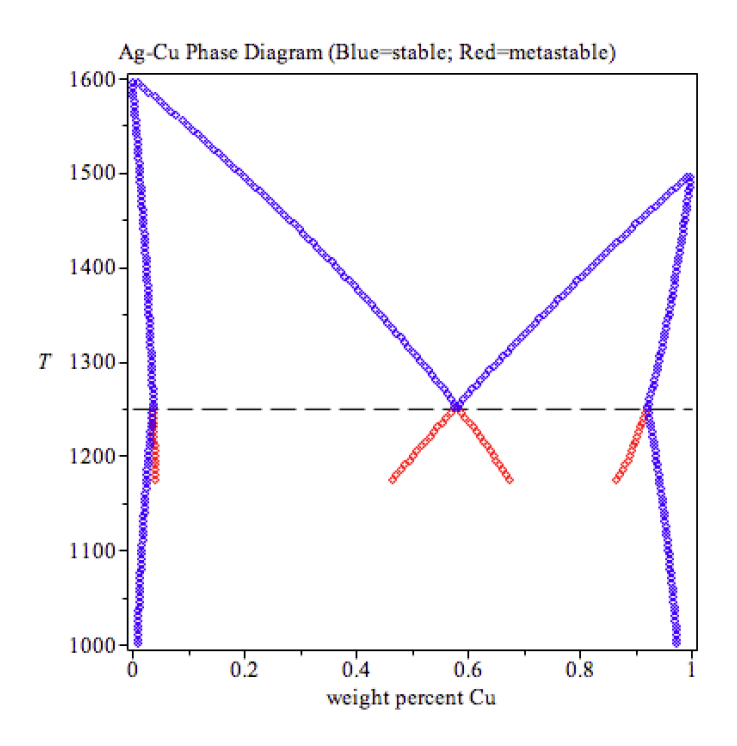


Figure 3.3: Silver-copper phase diagram

phased and l (or L) the liquid phase),

$$f_{exp}^{\alpha} \approx f(c_{eq}^{\alpha}) + \frac{\partial f(c_{eq}^{\alpha})}{\partial c} \left(c - c_{eq}^{\alpha} \right) + \frac{1}{2} \frac{\partial^2 f(c_{eq}^{\alpha})}{\partial c^2} \left(c - c_{eq}^{\alpha} \right)^2$$
(3.1)

where c_{eq}^{α} and the derivatives could be calculated directly from the experimental free energy curves. Equation 3.1 can simply be rearranged by completing the square into the form

$$f_{\text{parabolic}}^{\alpha} = \frac{A_{\alpha}}{2} \left(c - c_{min}^{\alpha} \right)^2 + B_{\alpha}$$
 (3.2)

By comparing the effective coefficients in Eq. (3.2) with the coefficients in Eq. (2.37) at each temperature, it is straightforward to define the coefficients in Eq. (2.42), which enter directly into the phase equations ². In practice it is often much more convenient

²It is noted that it is also possible to fitting the experimental free energy plots to second order in concentration (c) in piecewise intervals on 0 < c < 1. This will then lead to coefficients in Eq. (2.42) that change with temperature and concentration interval. In this case, the parabolic free energy based parameterization of the phase field model proposed here can be arbitrarily accurate to model complex solidification in nearly any engineering alloy.

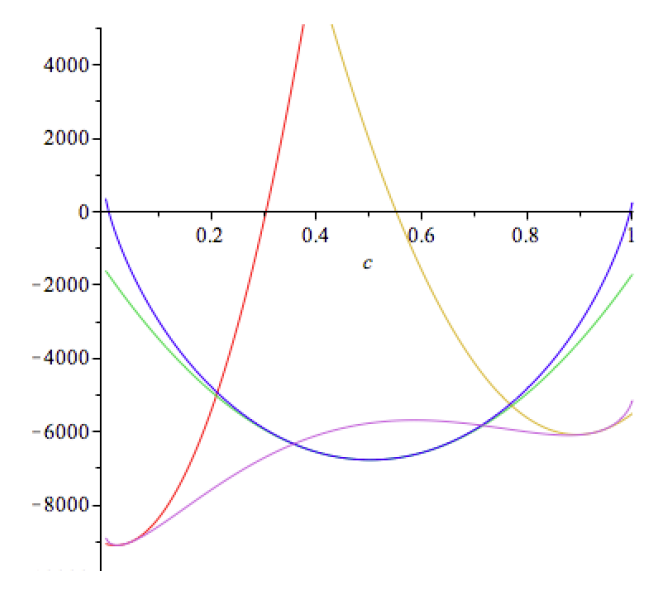


Figure 3.4: Experimental free energy (purple and dark purple) overlaied with fitted parabolic free energies (other colours) At T = 1230 K.

to do such algebraic manipulations of the free energy in algebraic software packages such as Maple or Mathematica, because in general the experimental free energies have relatively complicated expressions. Numerical fitting is also completely viable as well. The above procedure was applied to the experimental expressions provided to me for Ag-Cu. Figure 3.4 shown an example of parabolic fits of the liquid and two solid free energies to experimental liquid and solid free energies.

It is worth briefly noting now that parabolic fits may have short comings. For example in Fig 3.5, it seems the parabolic fitting we did in this thesis is quite reasonable for lower temperatures, below the eutectic temperature. At higher temperatures it is evident the parabola curvatures are quite high despite correctly capturing the correct equilibrium minima. Figure 3.6 shows the approximation of the Ag-Cu phase diagram in Fig. 3.3 re-built from the parabolic free energies whose coefficients are extracted by matching to the experimental free energies as shown in Fig. 3.4. (This is also the temperature used in simulations in section 3.3) It is further clear here that at higher temperature ranges the fitting scheme starts to break down. Another short coming of the fitting scheme used for this particular system is that on the β side of the phase diagram we restricted the range of available temperatures because,

52 ______ **3** Results

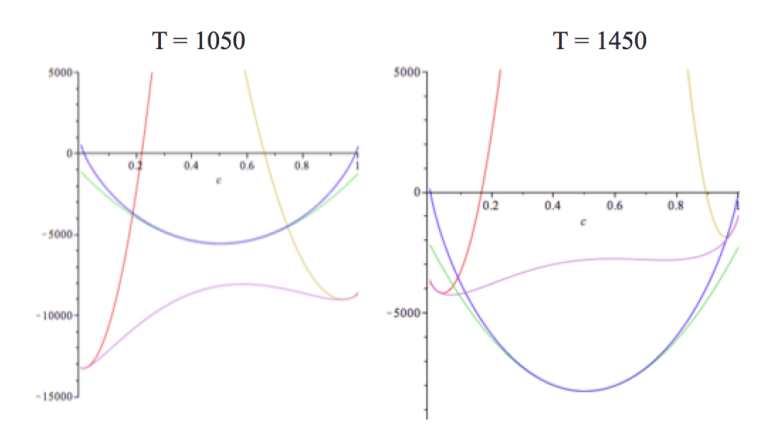


Figure 3.5: Comparison of how well the parabolic approximations are at two different temperatures. T = 1050 K (left) and T = 1450 K (right)

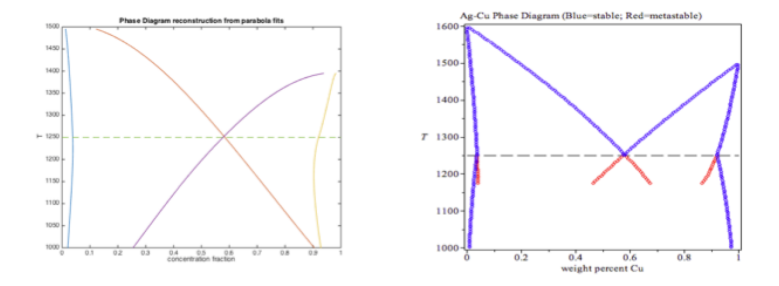


Figure 3.6: Side by side comparison of experimental (right) and approximately reconstructed phase diagram (left). Temperature reconstruction range was lowered to T=1500 as that is the higher limit for the β side of the phase diagram. The liquidus lines in this (left) case are extended for their full metastable projection

in the reconstruction process, Equation (2.41) returns imaginary numbers which is unphysical. Despite this however, the reconstruction is quite reasonable, recovering the correct eutectic temperature and seems to match quite well in the region studied in this thesis.

One possible remedy to this, is to essentially split the liquid free energies into a piece wise free energies such that you recover a seperate χ_{liq}^{eq} for each side of the phase. For this particular system, since the liquid free energy was quite symmetric, we had reasonable approximations in the lower temperature regime. But in the higher temperature regime we saw that the common tangent construction failed. Thus it may be possible to capture the full landscape by using the above method.

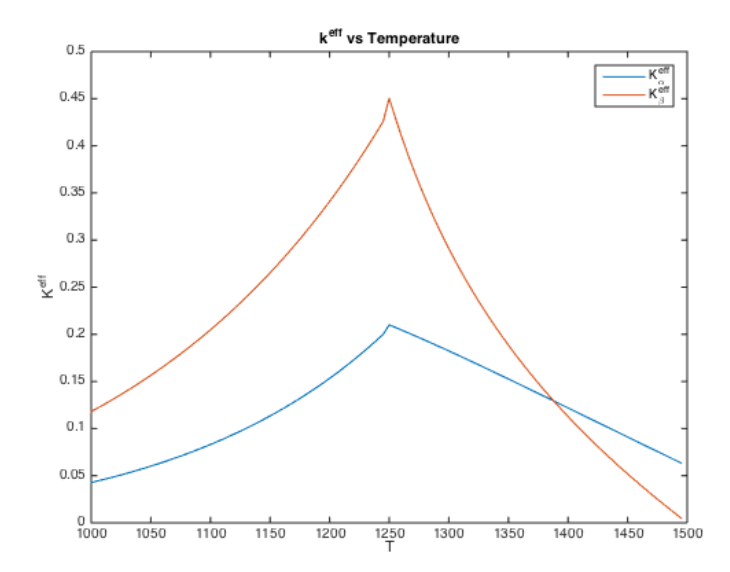


Figure 3.7: K^{eff} vs Temperature curves. A look at the liquid to solid curvature ratios at different temperatures. Note the inflection at the Eutectic temperature, which is when the system transition from stable to metastable

Another interesting finding for this fitting scheme is in Fig 3.7. Recall that this is the ratio of the liquid to solid parabolic curvatures. We find that there is an inflection at the *eutectic temperature* for the K^{eff} values. One could interpret this as a transition from a stable(right of inflection) to metastable(left) region, which makes sense since eutectic solidification (or perhaps, more generally, multi-phase solidification) is a metastable process until full equilibrium is reached.

3.2 Lamellar Eutectic Structures

3.2.1 qualitative features

Features of lamellar eutectics are explored here using the ideal binary phase diagram in Fig 3.1. The theory of steady state lamellar growth has been studied quite extensively, and could be found in sources such as. [2, 51]. One key topic explored theoretically has been the spacing or two-phase lamella in a eutectic solid front growing at a constant speed. It is well-known that a stable lamellar growth front will exhibit a sinusoidal

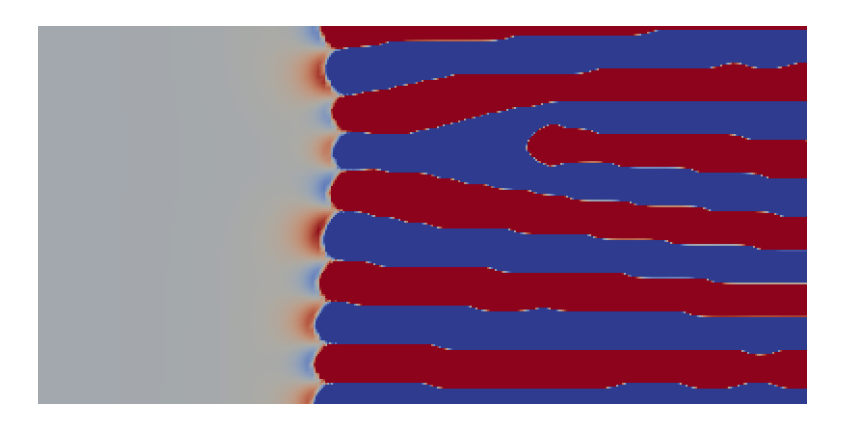


Figure 3.8: Lamellar front comprised of α phase (red) and β phase growing into an undercooled liquid. An elimination event of an α lamella due to instability is shown $\sim 3/4$ up the vertical direction.

profile in concentration. A typical example is shown in Fig. 3.8. This figure also shows the elimination of one of the lamellar phases due to an instability at the front (discussed further below). Under ideal conditions, the solute concentration across the lamellar front follows a sinusoidal distribution. Figure 3.9 shows this for two typical aligned lamella, such as this that appear in Fig. 3.8. Under such conditions, it is well known that the growth speed is linear with respect to the inverse square of the lamellar spacing. The latter result a hallmark result for eutectic solidification first derived by Jackson and Hunt [2]. Fig 3.10 shows this linear scaling from our simulations with the proposed model, and is in agreement with previous eutectic studies using a different type of phase-fraction-based model [50].

Another important physical feature of eutectic lamellar growth is the minimum undercooling concept. This principal states that stable eutectic growth will operate at (or near) a lamellar spacing such that the undercooling is minimized [51]. Instabilities form at arbitrarily large or small lamellar spacings. While a full quantitative treatment of this concept is beyond the scope of this thesis. Here, I demonstrate that these expected instabilities indeed arise in the model developed in this thesis. As lamellar spacing decreases, lamellar elimination is known to occur experimentally. This effect is also captured in our simulations, as shown in Fig 3.8. And for arbitrarily large spacing, oscillatory states take over as in Fig 3.11.

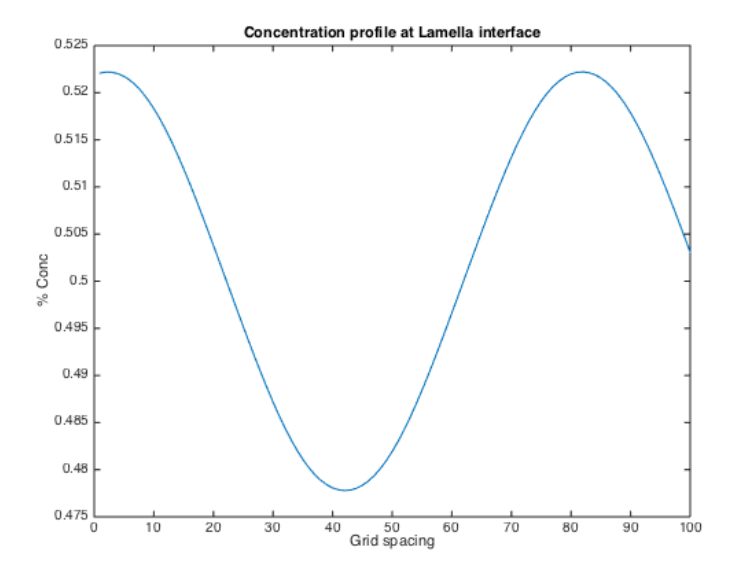


Figure 3.9: Example concentration profile across a lamellar front where high concentration is the β solid phase (see text) and low concentration is the α solid phase

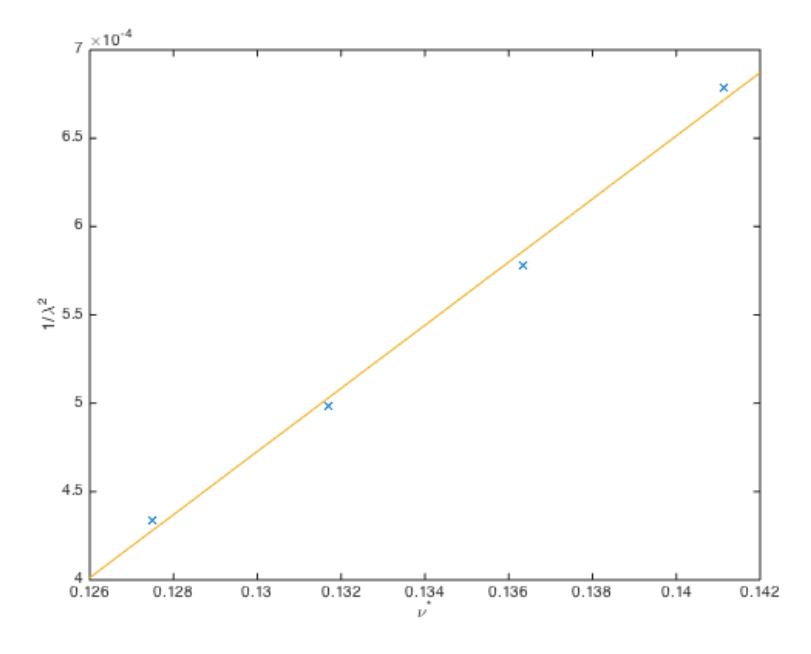


Figure 3.10: Linear scaling or inverse square distance $1/\lambda^2$ between two-phase lamella as a function of eutectic front speed ν^* . This result is consistent with the celebrated Jackson and Hunt scaling analysis [2]

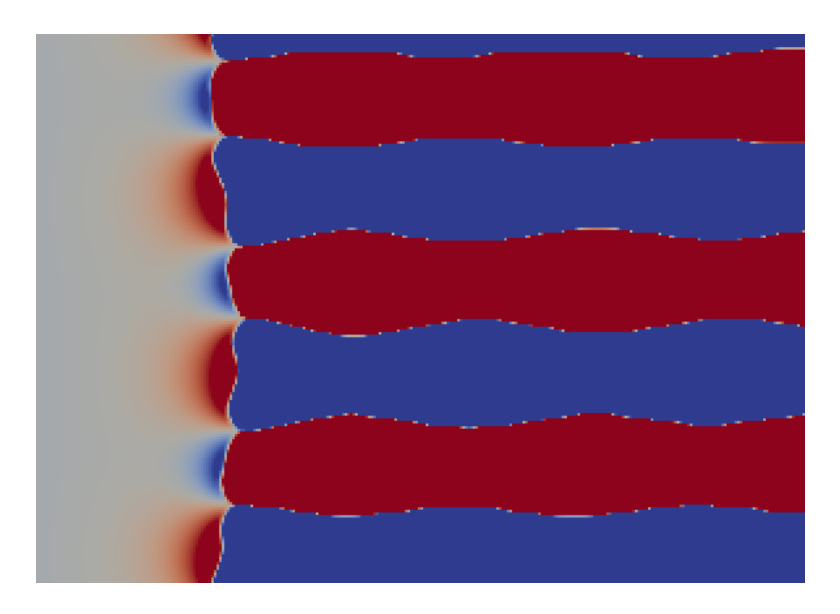


Figure 3.11: Oscillation modes of lamella due to instability due to the minimum undercooling concept

Figures 3.8, 3.11 and 3.12 also illustrate another well-known effect in eutectic solidification called *short circuit diffusion* between solid phase at the lamella growth front. This is a known process where the composition ahead of the α front is rich in β composition (and vice-versa); this coupled growth process can thought of as being symbiotic relationship where each phase contributes to the other's growth.

The results presented above will also be appearing in an upcoming publication by Greenwood et al that showcases and benchmarks the workings of a new 3D parallel adaptive mesh refinement code. A snapshot of the AMR mesh in 2D is shown in Fig. 3.12.

3.2.2 Numerical quantities used in simulations

The phase field parameters used for this particular simulation shown above were as follows: $w_{obs} = 55$, $W_{\alpha} = W_{\beta} = 1$, $\tau_{\alpha} = \tau_{\beta} = 1$, $\Delta x = 0.8$, $\Delta t = 0.032$, $\lambda = 3.59$, $\bar{D} = 2.25$, and in weight fraction, $c^{eq(\alpha)} = 0.0875$, $c^{eq(\alpha,l)} = 0.5833$, $c^{eq(\beta)} = 0.9125$, $c^{eq(\beta,l)} = 0.4167$, $c_{\infty} = 0.5$. In addition, an anti-trapping coefficient of $a_t = 1/2\sqrt{2}$. and a diagonal susceptibility tensor with an equal curvature parabolic model i.e. $k^{\text{eff}} = 1$ for all phases. The dimensionless supersaturations was $|\Omega| \approx 0.168$ for both

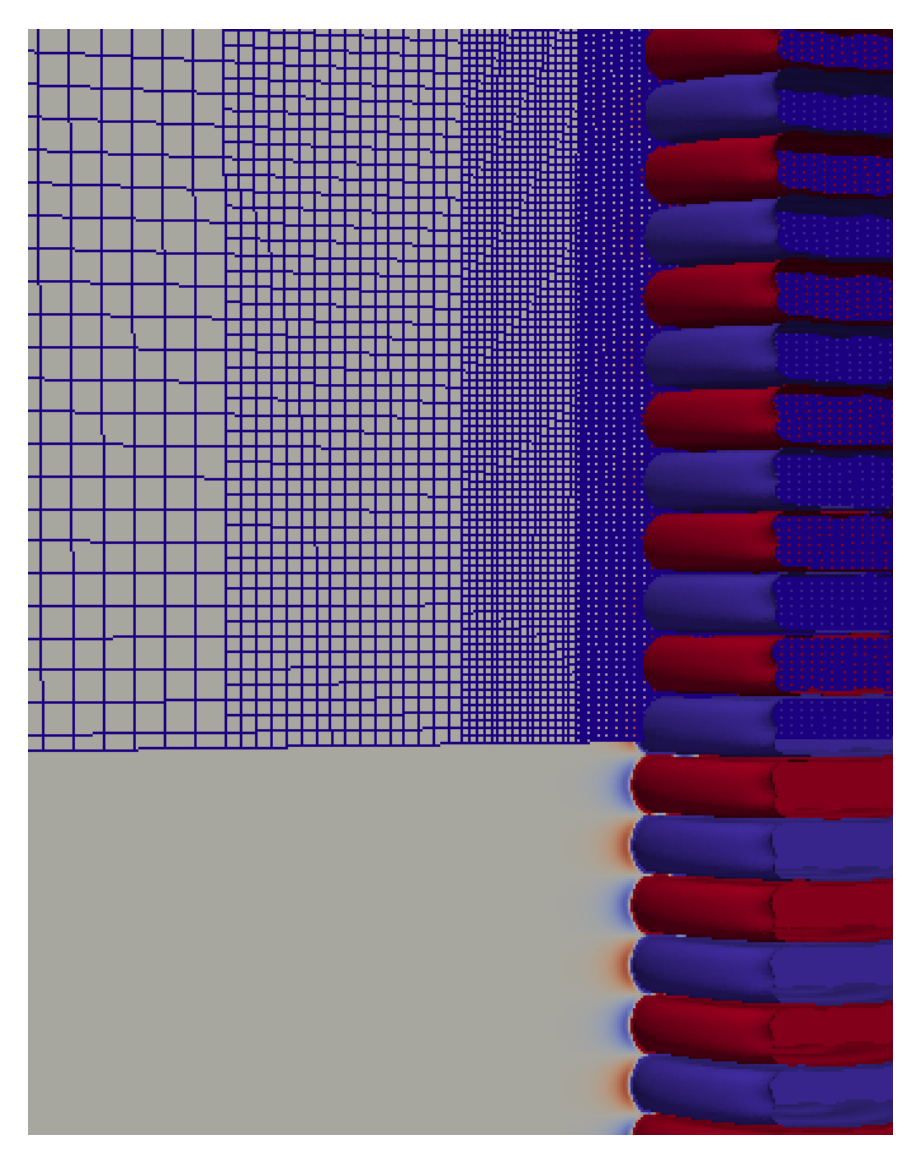


Figure 3.12: Stable 3D growth of lamellae growing in on an adaptive mesh. Zoom in of the total system is shown.

phases, in an isothermal quench. Initialization of the system is done initializing an array of alternating alpha-beta lamella which are interpolated (via the phase field) between their equilibrium chemical potential in the bulk and far-field liquid chemical potential. The initial chemical potential fields are done using Eqs 2.39 and 2.43 In the data of Fig. 3.10, similar parameters as above were used, except here several dimensionless supersaturations and spacings were explored. In this case, we also set $a_t = 0$ and set $q(\phi) = 1$ and $\lambda \approx 48$. These simulations were carried out at several lamellar spacings and several dimensionless supersaturations and grown until a steady-state velocity was measurable to display the resulting linear scaling law behaviour. Care was taken to ensure lamellae followed a regular growth pattern as explained in [51]

3.3 Homogeneous Two-Phase Nucleation

This section adds noise to the phase field model equations to study two-phase homogeneous nucleation and growth. Preliminary results are presented.

3.3.1 Implementation of order parameter noise

The implementation of the noise addition to each order parameter is done as follows: first for each phase α, β , an auxiliary 'ghost' order parameter field is set up for each phase. The purpose of a 'ghost' field is to fluctuate an ideal liquid devoid of any solid until a nucleus of that solid emerges, after which it "assigns" this ghost field (containing the nucleus) to an order parameter field that "lives" in the solidifying domain being tracked by the simulation. Ghost fields interact with the real grains in the physical system so that nucleated grains cannot overlap with existing grains, and are rejected through the phase field model's interaction potential terms. Conversely, real grains in the physical domain have no "awareness" of the ghost field. The noise for each phase's ghost field follows Guassian distributed noise (using the standard

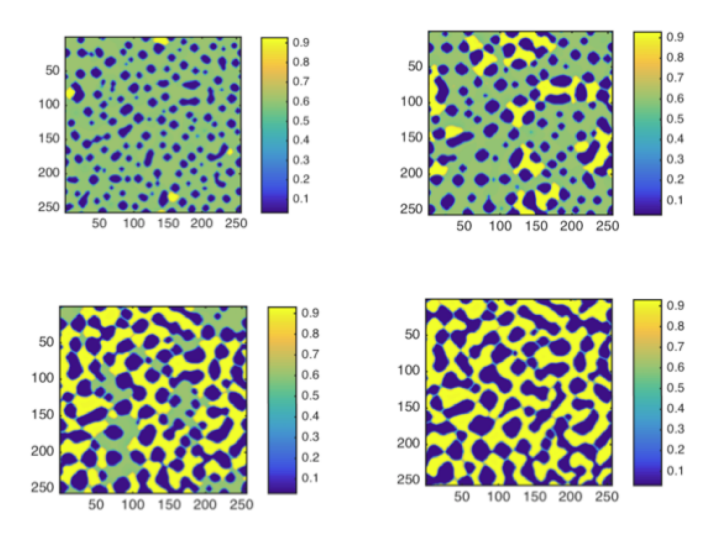


Figure 3.13: Top left to right, to bottom left to right: homogeneous nucleation of α (blue) at temperatures above the eutectic temperature, followed by inter-phase nucleation of $\beta(yellow)$. Parameter $\lambda=8.03$ and initial supersaturation of $U_{\alpha}\approx-0.21$. The dimensionless system size was (1862 $\bar{x}/\bar{d}_o)^2$ and the dimensionless time (scaled by \bar{D}/\bar{d}_o^2) was ≈ 35000 (top left), 79000(top right), 114000(bottom left), 158000(bottom right). Overbars represent scaling of space with W and time with τ

C++ library) and variance given by Equation (2.75). This noise term is added to the end of Equation (2.55), and every few iterations, the code checks if a phase has nucleated and assigns the phase to a new order parameter. This assignment frequency was every 10 time steps for these simulations in this thesis. It is found that results don't change if we further reduce this inspection frequency.

3.3.2 Demonstration of homogeneous nucleation

In this subsection, two-phase homogeneous nucleation was investigated for hypoeutectic concentration of the Ag-Cu alloy system in Fig. 3.3. Figure 3.13 shows an example of a typical nucleation process after an isothermal quench below the eutectic temperature for an alloy of average concentration of $c_{\infty} = 0.5wt\%Cu$. Time and space have been appropriately scaled to be dimensionless. For this system the following numerical set up was used: $\Delta x = 0.8W$, $\Delta t = 0.0006\tau \lambda = 8.03$, $\bar{D} = 5.03$, $\bar{d}_o = 0.11$, $\bar{\chi}_l^{eq} = 3.99$ (rescaled to be dimensionless), $k^{\alpha(\text{eff})} \approx 0.18$, $k_{\beta}^{\beta(\text{eff})} \approx 0.40$, $c_{min}^{\alpha} = 0.018$, $_{---}$ 3 Results

 $c_{min}^{liq}=0.502, c_{min}^{\beta}=0.895$, and a liquid phase far field composition, $c_{\infty}=0.5$. This far field composition puts the system in an hypocutectic-like set up, where $U_{\alpha}\approx$ -0.21 and $U_{\beta}\approx$ 0.123. A phase requires U<0 to be thermodynamically favourable to grow. Here, we expect α to nucleate first and β will be unable to nucleate until the liquid is saturated enough that the local U_{β} is favourable for it. This expectation is demonstrated in fig 3.13, which illustrates homogeneous two-phase nucleation and growth at an isothermal quench below the eutectice. The model's parabolic parameter extractions were done for the isothermal quench temperature T=1230 K in Ag-Cu phase diagram in Fig 3.3. It is noted that for time varying temperature changes, one would continuously feed pre-fitted parameters from the above procedure at each temperature.

The noise amplitude parameter $F_{exp} \approx 0.5$ in Eq. (2.76). To get this value we use experimental parameters for Silver. Stricly, each phase should have its own noise value, however we assume for simplicity that it is reasonable to use the same noise amplitude for both phases as the order of magnitudes would still be roughly the same. The following parameters were used to calculate Equation (2.78) and subsequently F_{exp} : $\Gamma_{\alpha} = 2.4 \times 10^{-7} m \cdot K$, $L_f = 11.3 \times 10^3 J/mol$, $T_m = 1600 K$, $\Delta c_{eq}^2 = 0.57 wt. fraction$, $\Omega_o = 10.2 cm^3/mol$. This value of the noise amplitude seems to be in quantitative agreement with [73, 74, 75]

3.3.3 λ invariance in nucleation

Figure 3.14 measure the solid fraction versus scaled(right) and unscaled (left) times for three values of the inverse nucleation barrier λ : 9.8, 8.8, and 8.0, and other parameters as in the data of Fig 3.13 with one exception; $\Delta x = 0.4W$ was used instead. Based on our theoretical discussions earlier in the thesis, λ parameter sets the interface width, and also the diffusional time scale of phase field simulations. This implies that in a simulation with a higher λ , the characteristic time step for solidification will be *larger* for larger value of λ . Correspondingly, the characteristic

spacial scale will also be larger in the simulation with the larger λ value. However, we expect that upon non-dimensionalization of all results, the λ -controlled space and time scale should make results independent of λ , i.e. independent of the materials nucleation barrier. The right plot of Fig 3.14 shows evidence of this dimensionless scaling as well as Fig 3.15 which shows, at approximately the same dimensionless space and time scale, the systems with different λ look similar. It is also worth noting the beginning region before the inflection - here the primary phase nucleates rapidly and the system reaches a temporary 'saturation' in solidification until the local super saturation, in other words, the driving force, in the liquid phase is enough to continue nucleating the secondary phase and so on.

Figure 3.16(left) shows results from 20 statistical runs from the simulation in Fig. 3.13. The typical amount of stochastic variance from run-to-run varies enough to require averaging over many ensembles to obtain meaningful results. Thus, this figure provided evidence to perform and average over 20 ensembles for 3 different λ in Fig 3.14. It goes without saying that further ensemble averaging would even further improve the convergence.

It is noted that, physically, $U_{\alpha} \approx -0.21$, corresponds to a fairly high cooling rate. This, coupled with large λ , would contribute to spurious non-zero kinetic effects that emerge to the eventual breakdown of the asymptotic analysis that maps the proposed phase field model onto the corresponding sharp interface model of alloy solidification in Eqs. (2.63), which allows use of the relationships in Eqs. (2.64) in the first place. That may be a possible reason why the solid fraction rate don't completely collapse on to eachother. Another possible explanation is that, similar to how large Δx values affect dimensionless tip velocity convergence (for example see [7]), it is possible that convergence would be better with a lower Δx than used in these simulations. A potential follow up of this apparent convergence could be examining a variety of λ , and undercoolings.

62 3 Results

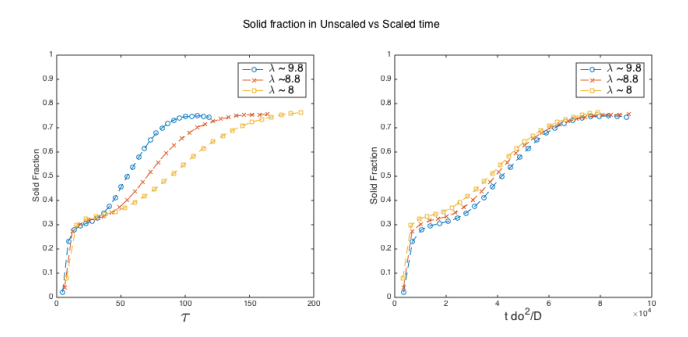


Figure 3.14: Solid fraction comparison in unscaled (left) and scaled (right) time, indicating the effect of λ as a convergence parameter, averaged over 20 runs for each λ

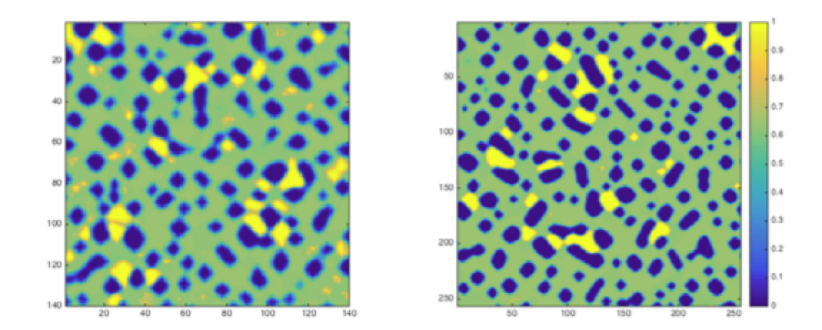


Figure 3.15: Left $\lambda=14.7$, dimensionless time ≈ 47000 , dimensionless space $\approx 1867^2$. Right $\lambda=8.03$, dimensionless time ≈ 45000 , dimensionless space $\approx 1862^2$. The higher λ 's concentration map is essentially a 'zoom' in of the lower λ because of the nature of λ 's spatial scaling

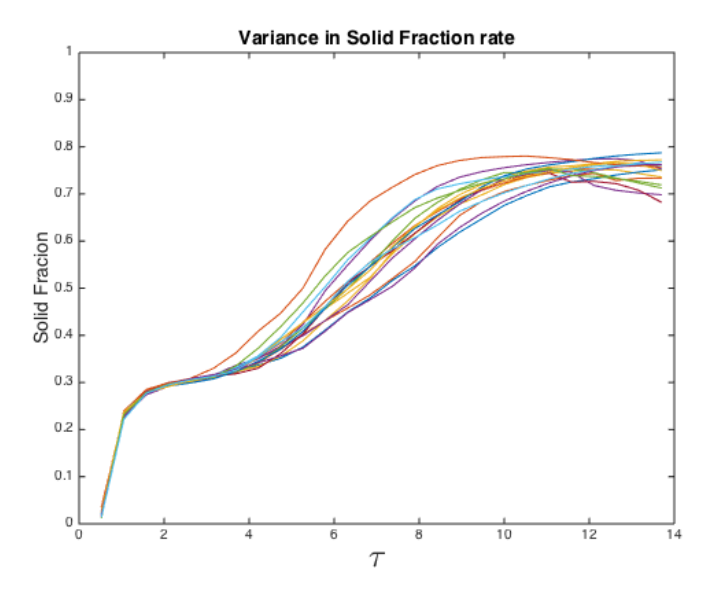


Figure 3.16: Typical variance in 20 solid fraction simulations.

4

CONCLUSIONS

This thesis was largely devoted to deriving and demonstrating a new multi-order parameter based phase field model for multi-phase solidification of complex alloys with multiple solute components. The derivation is novel in two ways. First, it is based in the grand potential. In this ensemble, the dynamics of solidification are described in terms of chemical potentials and not concentrations as is done customarily in most order-parameter type phase field models. This feature allows easy control of thermodynamic driving forces to experimental properties of material phases it also allows complete de-coupling of the properties through the mesoscale interface (W)from solute variation. Second, the modelling tool derived here is physically consistent compared to some solidification models in the literature that replace order parameters with phase fractions. The latter type of models add constraints to the dynamics and can lead to artificial phase adsorption at inter-phase junctions. Finally, by fitting the free energy of any phase to quadratic order in concentration, we showed that the thermodynamic driving forces that drive changes in chemical potentials and order can be compactly cast as a second order expansion in local supersaturations U_{α} ; the U_{α} are elegant variables to work in as it depends only the susceptibility of a phase α and its equilibrium chemical potential with its melt. Our formulation in terms of U_{α} (Eqs. (2.51) and (2.55)) allows simulations to deviate from equilibrium significantly. It also has the very appealing feature of reducing the model to simpler (and lowerorder) phase field models in the literature for which the parameter mapping of various materials properties has been well established.

64 Conclusions

In addition to the mesoscale equations of motions, we also added noise in our theory to account for fluctuations and nucleation phenomena -one of the main topics that the model was created to investigate. We work throughout in units where space scales like the interface width, where time scales like the time scale of order parameter fluctuations and where energy scale like $k_BT\bar{\rho}$ ($\bar{\rho}$ is the average density of the material). As such, we are able to non-dimensionalise the noise and parameterize it in terms of the inverse [dimensionless] nucleation barrier hight, the same parameter that also enters the coupling between supersaturation and any order parameter. In fact, our dimensionless model has three types of parameters: dimensionless diffusion coefficient, the inverse nucleation barrier (assumed the same for each solid phase) and the equilibrium susceptibility (i.e. curvature of its free energy)and chemical potential(s) of each phase. Through dimensional analysis we illustrate in this work how the effect of λ can be consistently scaled out of phase field simulation results. This is important when comparing the role of mesoscale parameters on the kinetics of solidification microstructure evolution.

Simulations are performed to demonstrate our model on two materials systems. The first is an ideal binary eutectic alloy and the second a Ag-Cu alloy. In both cases the parameters of our model equations were fit and simulations run to test two specific situations in two-phase solidification. Briefly, the effectiveness and shortcomings of the parabolic fitting scheme are highlighted as well. It is also found that there is a unique inflection in the k^{eff} values (the ratio of liquid to solid curvatures) with temperature, which describe an expected stable-metastable transition at the eutectic temperature.

The first set of simulations was the spacing and morphology of eutectic lamellar cells. Here we demonstrated such physical features such as short circuit diffusion and lamellar instabilities that give rise to oscillation and elimination behaviours. We also demonstrate a quantitative analysis namely the classic Jackson and Hunt linear scaling law of inverse lamellar spacing with eutectic growth speed. This further

validates our new model.

We next explored homogeneous nucleation of two-phases in the so-called hypo eutectic region of the eutectic phase diagram. When we quench below the eutectic, we observe first primary phase nucleation (α) followed later by secondary phase (β) nucleation in the remaining liquid. This sequence is in accord with the thermodynamic driving forces, which are larger for α grains than for β grains in the hypo-eutectic part of the phase diagram. We tracked the solid fraction versus time of the two-phase nucleation process for different values of λ (i.e., inverse nucleation barrier). From the rate of solid fraction curves, we find evidence that suggests the noise-induced nucleation does indeed work self consistently in the model. Moreover, when time and space are scaled by physical length scales in the problem, that are here "tuneable" through λ , it appears that there is apparent convergence in the behaviour of the solid fraction versus time behaviour that is independent of λ ; presumably, though this type of scaling the kinetics of solid fraction versus time depend only on the thermodynamic driving force (i.e. the supersaturation of the original liquid), and other materials parameters.

Going forward, the accessible nature of the parabolic model described here is readily extensible to complex multi-component alloys as long as the correct thermodynamic free energies of their possible phases are characterizable theoretically or experimentally e.g. with databases such as CALPHAD. Such a model, mixed with adaptive mesh refinement algorithms such as the one my model has been used to develop, can lead to very practical and experimentally relevant applications of the model developed herein. In addition, a heterogeneous nucleation model should incorporated alongside the homogeneous nucleation mechanism incorporated here. This will alloy more realistic simulations of multi-phase solidification at slower solidification rates and lower temperature quenches. This will allow a more complete and self-consistent study of emerging non-equilibrium processes associated with rapid solidification and additive manufacturing to be studied.

\mathbf{A}

Phase Field Dynamics for General Complex Alloy Systems

A.1 Multi-Phase, Multi-Component Alloys with Quadratic Free Energy Forms

Here we generalize the Section (2.6) for (n-1) components and N solid phases, indexed with α solidifying from a melt, denoted here by L. Our starting point is again Eqs. (2.33) and (2.36). A phase, in general, will be denoted by ϑ . It is assumed that the free energy of a phase can be expanded to quadratic order near some reference concentrations. While real material typically has complex functional forms to describe their free energy, much of the physics of multi-component solidification can be captured with this order of approximation of the free energy [76].

Free energy and susceptibility of a single phase

We begin by expressing the free energy of a phase ϑ by the quadratic form

$$f^{\vartheta}(c_{1}, c_{2}, \cdots, c_{n-1}) = \frac{1}{2} \sum_{i=1}^{n-1} \sum_{j=1}^{n-1} A_{ij}^{\vartheta} \left(c_{i} - \bar{c}_{i}^{\vartheta} \right) \left(c_{j} - \bar{c}_{j}^{\vartheta} \right) + \sum_{j=1}^{n-1} B_{j}^{\vartheta} \left(c_{j} - \bar{c}_{j}^{\vartheta} \right) + D^{\vartheta},$$
(A.1)

where c_i denotes the concentration of component i and A_{ij}^{ϑ} , \bar{c}_i^{ϑ} , B_j^{ϑ} and D_i^{ϑ} are fitting parameter that are possibly temperature dependent and in principle extractable from thermodynamic databases like Thermocalc/CALPHAD, at least for select ranges of

coexistence between some solid phases and liquid. This is a reasonable form to describe a wide range of solid alloy phases [26, 76]. From Eq. (A.1) the chemical potential in each phase is given by

$$\mu_m^{\vartheta} = \frac{\partial f^{\vartheta}}{\partial c_m} = \sum_{j=1}^{n-1} A_{mj}^{\vartheta} \left(c_j - \bar{c}_j^{\vartheta} \right) + B_m^{\vartheta} \tag{A.2}$$

and thus

$$\frac{\partial \mu_m^{\vartheta}}{\partial c_l} = \frac{\partial^2 f^{\vartheta}}{\partial c_l \partial c_m} = A_{ml}^{\vartheta} \tag{A.3}$$

for any concentration. From Eq. (A.3), we define the elements of the inverse susceptibility matrix of a phase by

$$[\chi^{\vartheta}]_{ij}^{-1} \equiv \frac{\partial \mu_i^{\vartheta}}{\partial c_j} = A_{ij}^{\vartheta}, \tag{A.4}$$

For quadratic forms, the matrix $[A^{\vartheta}]$ is symmetric, which makes its inverse,

$$[\chi^{\vartheta}] = \begin{bmatrix} \frac{A_{22}^{\vartheta}}{A_{11}^{\vartheta} A_{22}^{\vartheta} - (A_{12}^{\vartheta})^{2}} & -\frac{A_{12}^{\vartheta}}{A_{11}^{\vartheta} A_{22}^{\vartheta} - (A_{12}^{\vartheta})^{2}} \\ -\frac{A_{12}^{\vartheta}}{A_{11}^{\vartheta} A_{22}^{\vartheta} - (A_{12}^{\vartheta})^{2}} & \frac{A_{11}^{\vartheta}}{A_{11}^{\vartheta} A_{22}^{\vartheta} - (A_{12}^{\vartheta})^{2}} \end{bmatrix}$$
(A.5)

also a symmetric matrix.

Vector notation and transformations between concentrations and chemical potentials

In what follows, bold letters between square braces will denote $(n-1) \times (n-1)$ matrices and vector arrows will denotes $(n-1) \times 1$ column or row matrices. It is noted for future reference that

$$B_m^{\vartheta} = \mu_m^{\vartheta}(c_j = \bar{c}_j^{\vartheta}) \equiv \bar{\mu}_m^{\vartheta} \tag{A.6}$$

It will prove very useful to couch the multi-order parameter model in matrix notation rather than index notation. An $(n-1) \times 1$ vector is represented by a vertical column of numbers and its transpose by a corresponding horizontal row of numbers. Thus, the n-1 concentrations can be equivalently expressed as

$$\vec{c} = \begin{bmatrix} c_1 \\ c_2 \\ \vdots \\ c_{n-1} \end{bmatrix}, \quad \vec{c}^T = [c_1, c - 2, \cdots, c_{n-1}]$$
(A.7)

Following this notation, we further define the following vectors to be used below,

$$\vec{\mu}^T = [\mu_1, \mu_2, \cdots, \mu_{n-1}]$$
 (A.8)

$$(\vec{c}^{\vartheta})^T = [\vec{c}_1^{\vartheta}, \vec{c}_2^{\vartheta}, \cdots, \vec{c}_{n-1}^{\vartheta}]$$
(A.9)

$$(\vec{\mu}^{\vartheta})^T = [\bar{\mu}_1^{\vartheta}, \bar{\mu}_2^{\vartheta}, \cdots, \bar{\mu}_{n-1}^{\vartheta}] \tag{A.10}$$

$$\Delta \vec{C}^T \equiv (\vec{c}^T - (\vec{c}^\vartheta)^T) = [c_1 - \bar{c}_1^\vartheta, c_2 - \bar{c}_2^\vartheta, \cdots, c_{n-1} - \bar{c}_{n-1}^\vartheta]$$
(A.11)

$$\Delta \vec{\mu}^T \equiv (\vec{\mu}^T - (\vec{\mu}^\vartheta)^T) = [\mu_1 - \bar{\mu}_1^\vartheta, \mu_2 - \bar{\mu}_2^\vartheta, \cdots, \mu_{n-1} - \bar{\mu}_{n-1}^\vartheta]$$
 (A.12)

In terms of the above definitions, the free energy of phase ϑ (Eq. (A.1)) can be written as

$$f^{\vartheta}(\vec{c}) = \frac{1}{2} \Delta \vec{C}^T [\boldsymbol{\chi}^{\vartheta}]^{-1} \Delta \vec{C} + \vec{\mu}^{\vartheta} \cdot \Delta \vec{C} + \vec{D}^{\vartheta}$$
 (A.13)

where $[\chi^{\vartheta}]$ is matrix notation for the susceptibility matrix in Eq. (A.4).

Equation (A.2) can be used to define a transformation for commuting between concentration and chemical potential variables, given by

$$\Delta \vec{\mu} = \vec{\mu} - \vec{\bar{\mu}}^{\vartheta} = [\boldsymbol{\chi}^{\vartheta}]^{-1} \Delta \vec{C} \tag{A.14}$$

$$\Delta \vec{C} = \vec{c} - \vec{\bar{c}}^{\vartheta} = [\boldsymbol{\chi}^{\vartheta}] \, \Delta \vec{\mu},\tag{A.15}$$

where it is recalled that the components of $\vec{\bar{\mu}}^{\vartheta}$ are defined by Eq. (A.6).

Grand potential and concentration of a single phase

The grand potential of phase ϑ is given by

$$\omega^{\vartheta} = f^{\vartheta}(c_1, c_2, \cdots, c_{n-1}) - \sum_{j=1}^{n-1} \mu_j \, c_j = f^{\vartheta}(\vec{c}) - \vec{\mu} \cdot \vec{c}$$
 (A.16)

Substituting Eq. (A.15) for $\Delta \vec{C}$ in Eq. (A.13), and using Eq. (A.15) to write $\vec{\mu} \cdot \vec{c} = \vec{\mu}^T [\chi^{\vartheta}] \Delta \vec{\mu} + \vec{\mu} \cdot \vec{c}^{\vartheta}$, tranforms Eq. (A.16) to

$$\omega^{\vartheta}(\vec{\mu}) = -\frac{1}{2} \Delta \vec{\mu}^T [\boldsymbol{\chi}^{\vartheta}] \Delta \vec{\mu} - (\vec{c}^{\vartheta})^T \vec{\mu} + \vec{D}^{\vartheta}$$
(A.17)

In arriving at Eq. (A.17), use was made of the fact that the scalar $\vec{\mu} \cdot \vec{c}^{\vartheta}$ satisfies

$$\vec{\mu} \cdot \vec{c}^{\vartheta} = \vec{\mu}^T \, \vec{c}^{\vartheta} = (\vec{c}^{\vartheta})^T \, \vec{\mu}, \tag{A.18}$$

and similarly for any other scalar forms. Equation (A.17) is the vector analougue of Eq. (2.44). From Eq. (A.17) the concentration corresponding to phase ϑ is given by

$$\vec{c}^{\vartheta}(\vec{\mu}) = -\frac{\partial \omega^{\vartheta}}{\partial \vec{\mu}} = [\chi^{\vartheta}] \Delta \vec{\mu} + \vec{\bar{c}}^{\vartheta}$$
(A.19)

The reader can validate this result by writing Eq. (A.17) in index form and carrying out the differentiation $-\partial \omega^{\vartheta}/\partial \mu_i$, and similarly for any other equation written in matrix form.

It will be convenient to define the minimum, $\vec{c}_{\vartheta}^{\, \text{min}}$, of the quadratic form of Eq. (A.1). Setting $\partial f^{\vartheta}/\partial \vec{c} = 0$ gives

$$\vec{c}_{\vartheta}^{\min} = \vec{c}^{\vartheta} - [\boldsymbol{\chi}^{\vartheta}] \, \vec{\mu}^{\vartheta} \tag{A.20}$$

Substituting Eq. (A.20) in Eq. (A.19) gives an alternate form for the phase concentration,

$$\vec{c}^{\vartheta}(\vec{\mu}) = [\chi^{\vartheta}]\vec{\mu} + \vec{c}_{\vartheta}^{\min} \tag{A.21}$$

Multi-phase concentration, susceptibility and concentration difference

For the case of a multi-phase system, Eq. (2.29) can be used to find the phase-interpolated form of the concentration of each component. This is expressed in vectorial form as

$$\vec{c}(\vec{\phi}, \vec{\mu}) = \sum_{\alpha} h_{\alpha}(\vec{\phi}) \left([\boldsymbol{\chi}^{\alpha}] \vec{\mu} + \vec{c}_{\alpha}^{\min} \right) + \left\{ 1 - \sum_{\alpha} h_{\alpha}(\vec{\phi}) \right\} \left([\boldsymbol{\chi}^{L}] \vec{\mu} + \vec{c}_{L}^{\min} \right)$$
(A.22)

Equation (A.22) can be further simplified by defining

$$\Delta \vec{C}_{\alpha} = \vec{c}_{L}^{\min} - \vec{c}_{\alpha}^{\min} \tag{A.23}$$

Rearranging Eq. (A.22) and using Eq. (A.23) gives

$$\vec{c}(\vec{\phi}, \vec{\mu}) = \left\{ [\boldsymbol{\chi}^L] - \sum_{\alpha} \left([\boldsymbol{\chi}^L] - [\boldsymbol{\chi}^{\alpha}] \right) h_{\alpha}(\vec{\phi}) \right\} \vec{\mu} - \sum_{\alpha} \Delta \vec{C}_{\alpha} h_{\alpha}(\vec{\phi}) + \vec{c}_L^{\min}$$
 (A.24)

Defining an effective partition matrix $[\mathbf{K}^{\alpha}]$ by

$$[\mathbf{K}^{\alpha}] = [\mathbf{\chi}^L]^{-1} [\mathbf{\chi}^{\alpha}], \tag{A.25}$$

the multi-phase concentration can be written as

$$\vec{c}(\vec{\phi}, \vec{\mu}) = [\boldsymbol{\chi}^L] \left\{ \mathbf{I} - \sum_{\alpha} \left(\mathbf{I} - [\boldsymbol{K}^{\alpha}] \right) h_{\alpha}(\vec{\phi}) \right\} \vec{\mu} - \sum_{\alpha} \Delta \vec{C}_{\alpha} h_{\alpha}(\vec{\phi}) + \vec{c}_L^{\min}, \quad (A.26)$$

where \mathbf{I} denotes the identity matrix. Equation (A.26) is the matrix analogue of Eq. (2.46).

Through the concentration, the susceptibility of a multi-phase system is found by Eq. (2.30), i.e., $\partial c_i/\partial \mu_j$. In vector form, this becomes

$$[\boldsymbol{\chi}] = \frac{\partial \vec{c}}{\partial \vec{\mu}} = [\boldsymbol{\chi}^L] \left\{ \mathbf{I} - \sum_{\alpha} \left(\mathbf{I} - [\boldsymbol{K}^{\alpha}] \right) h_{\alpha}(\vec{\phi}) \right\}$$
(A.27)

Using Eq. (A.21), and making use of Eq. (A.25), we can also compactly express the concentration difference $\vec{c}^L(\vec{\mu}) - \vec{c}^{\alpha}(\vec{\mu})$ between phases as

$$\vec{c}^{L}(\vec{\mu}) - \vec{c}^{\alpha}(\vec{\mu}) = \Delta \vec{C}_{\alpha} + [\boldsymbol{\chi}^{L}] \left\{ \mathbf{I} - [\boldsymbol{K}^{\alpha}] \right\} \vec{\mu}, \tag{A.28}$$

which is the matrix analogue of Eq. (2.49). Equation (A.28) will be relevant to the chemical potential diffusion equation.

It is instructive to re-cast Equation (A.28) into a more convenient form as follows. Consider that we are in a range of temperature such that for each local chemical potential $\vec{\mu}$ (or nominal composition) the solid phase α can co-exist, stably or metastably, with the liquid phase (L). As such, the μ_{n-1}^{eq} can be deduced from local conditions Evaluating the phase concentration in Eq. (A.21) at the set of $\mu_{\alpha(i)}^{\text{eq}}$, $i = 1, \dots, n-1$ defines the corresponding equilibrium concentrations of the coexisting liquid (L) and solid (α) , i.e.,

$$\vec{c}_{\text{eq}}^{\vartheta} = [\boldsymbol{\chi}^{\vartheta}] \vec{\mu}_{\alpha}^{\text{eq}} + \vec{c}_{\vartheta}^{\text{min}}, \quad \vartheta = L, \alpha$$
(A.29)

Writing Eq. (A.29) for liquid (L) and solid (α), and subtracting the two results gives

$$\Delta \vec{C}_{\alpha} = \Delta \vec{C}_{eq}^{\alpha} - [\boldsymbol{\chi}^{L}] \left\{ \mathbf{I} - [\boldsymbol{K}^{\alpha}] \right\} \vec{\mu}_{\alpha}^{eq}, \tag{A.30}$$

where

$$\Delta \vec{C}_{\rm eq}^{\alpha} \equiv \vec{c}_{\rm eq}^{\ L} - \vec{c}_{\rm eq}^{\ \alpha} \tag{A.31}$$

Substituting Eq. (A.30) into Eq. (A.28) and re-arranging reduces $\vec{c}^L(\vec{\mu}) - \vec{c}^{\alpha}(\vec{\mu})$ to

$$\vec{c}^{L}(\vec{\mu}) - \vec{c}^{\alpha}(\vec{\mu}) = \Delta \vec{C}_{eq}^{\alpha} + [\boldsymbol{\chi}^{L}] \left\{ \mathbf{I} - [\boldsymbol{K}^{\alpha}] \right\} (\vec{\mu} - \vec{\mu}_{\alpha}^{eq})$$
(A.32)

Grand potential driving force for multi-phase solidification

The final quantity we need to derive the phase field equations we seek in this subsection is the driving force for each order parameter (phase) i.e., $\omega^L(\vec{\mu}) - \omega^\alpha(\vec{\mu})$. Using Eq. (A.17) to evaluate the grand potential of each phase gives,

$$\omega^{L}(\vec{\mu}) - \omega^{\alpha}(\vec{\mu}) = -\frac{1}{2}\vec{\mu}^{T}[\boldsymbol{\chi}^{L}]\vec{\mu} + \frac{1}{2}\vec{\mu}^{T}[\boldsymbol{\chi}^{L}]\vec{\mu}^{L} + \frac{1}{2}(\vec{\mu}^{L})^{T}[\boldsymbol{\chi}^{L}]\vec{\mu} - \frac{1}{2}(\vec{\mu}^{L})^{T}[\boldsymbol{\chi}^{L}]\vec{\mu}^{L} + \frac{1}{2}\vec{\mu}^{T}[\boldsymbol{\chi}^{\alpha}]\vec{\mu} - \frac{1}{2}\vec{\mu}^{T}[\boldsymbol{\chi}^{\alpha}]\vec{\mu}^{\alpha} - \frac{1}{2}(\vec{\mu}^{\alpha})^{T}[\boldsymbol{\chi}^{\alpha}]\vec{\mu} + \frac{1}{2}(\vec{\mu}^{\alpha})^{T}[\boldsymbol{\chi}^{\alpha}]\vec{\mu}^{\alpha} - (\vec{c}^{L} - \vec{c}^{\alpha})^{T}\vec{\mu} + (\vec{D}^{L} - \vec{D}^{\alpha})$$
(A.33)

Several tedious "clean-up" steps are required to simplify Eq. (A.33). The first is to use Eq. (A.20) to write

$$(\vec{c}^L - \vec{c}^\alpha)^T \vec{\mu} = (\Delta \vec{C}_\alpha)^T \vec{\mu} + (\vec{\mu}^L)^T [\boldsymbol{\chi}^L] \vec{\mu} - (\vec{\mu}^\alpha)^T [\boldsymbol{\chi}^\alpha] \vec{\mu}$$
(A.34)

The second is to recall that, by definition, $\omega^L(\vec{\mu}_{\alpha}^{\text{eq}}) = \omega^{\alpha}(\vec{\mu}_{\alpha}^{\text{eq}})$, which, using Eq. (A.17) allows us to calculate $\vec{D}^L - \vec{D}^{\alpha}$, yielding

$$\vec{D}^{L} - \vec{D}^{\alpha} = -\frac{1}{2} (\vec{\mu}_{\alpha}^{\text{eq}})^{T} [\boldsymbol{\chi}^{\alpha}] \vec{\mu}_{\alpha}^{\text{eq}} + \frac{1}{2} (\vec{\mu}_{\alpha}^{\text{eq}})^{T} [\boldsymbol{\chi}^{\alpha}] \vec{\mu}^{\alpha} + \frac{1}{2} (\vec{\mu}^{\alpha})^{T} [\boldsymbol{\chi}^{\alpha}] \vec{\mu}^{\text{eq}} - \frac{1}{2} (\vec{\mu}^{\alpha})^{T} [\boldsymbol{\chi}^{\alpha}] \vec{\mu}^{\alpha} + \frac{1}{2} (\vec{\mu}^{\alpha})^{T} [\boldsymbol{\chi}^{\alpha}] \vec{\mu}^{\text{eq}} - \frac{1}{2} (\vec{\mu}^{\alpha})^{T} [\boldsymbol{\chi}^{L}] \vec{\mu}^{L} - \frac{1}{2} (\vec{\mu}^{L})^{T} [\boldsymbol{\chi}^{L}] \vec{\mu}^{\text{eq}} + \frac{1}{2} (\vec{\mu}^{L})^{T} [\boldsymbol{\chi}^{L}] \vec{\mu}^{L} + (\vec{c}^{L} - \vec{c}^{\alpha})^{T} \vec{\mu}^{\text{eq}}$$

$$(A.35)$$

When Eq. (A.34) and Eq. (A.35) are inserted in the last line of Eq. (A.33), the expression $(\vec{c}^L - \vec{c}^\alpha)^T \vec{\mu}_\alpha^{\text{eq}} - (\Delta \vec{C}_\alpha)^T \vec{\mu}$ emerges, which we need to simplify further. The second terms in this expression is derived directly from Eq. (A.29). The first

term is found by equating the expression for $\vec{c}_{\vartheta}^{\min}$ from Eq. (A.20) and Eq. (A.29). Proceeding thus, this expression becomes,

$$(\vec{c}^L - \vec{c}^\alpha)^T \vec{\mu}_\alpha^{\text{eq}} - (\Delta \vec{C}_\alpha)^T \vec{\mu} = -(\vec{\mu}_\alpha^{\text{eq}})^T ([\boldsymbol{\chi}^L] - [\boldsymbol{\chi}^\alpha]) \vec{\mu}_\alpha^{\text{eq}}$$

$$+ (\vec{\mu}_\alpha^{\text{eq}})^T ([\boldsymbol{\chi}^L] - [\boldsymbol{\chi}^\alpha]) \vec{\mu}$$

$$+ (\vec{\mu}^L)^T [\boldsymbol{\chi}^L] \vec{\mu}_\alpha^{\text{eq}} - (\vec{\mu}^\alpha)^T [\boldsymbol{\chi}^\alpha] \vec{\mu}_\alpha^{\text{eq}} - (\Delta \vec{C}_{\text{eq}}^\alpha)^T (\vec{\mu} - \vec{\mu}_\alpha^{\text{eq}})$$

$$(A.36)$$

Substituting Eq. (A.34) and Eq. (A.35) into Eq. (A.33) and making use of Eq. (A.36), finally gives, after tedious term-collecting,

$$\omega^{L}(\vec{\mu}) - \omega^{\alpha}(\vec{\mu}) = -\frac{1}{2}(\vec{\mu} - \vec{\mu}_{\alpha}^{\text{eq}})^{T} \left([\boldsymbol{\chi}^{L}] - [\boldsymbol{\chi}^{\alpha}] \right) (\vec{\mu} - \vec{\mu}_{\alpha}^{\text{eq}}) - (\Delta \vec{C}_{\text{eq}}^{\alpha})^{T} (\vec{\mu} - \vec{\mu}_{\alpha}^{\text{eq}})$$
(A.37)

Casting the driving force in term of supersaturations

It is instructive to re-cast Eq. (A.37) in a form that is more easily comparable to the form of the binary model in the previous section. We define a reduced supersaturation vector \vec{U}_{α} associated with each phase by

$$\vec{U}_{\alpha} = \frac{\left[\chi^{L}\right]}{\left|\Delta\vec{C}_{\text{eq}}^{\alpha}\right|} \left(\vec{\mu} - \vec{\mu}_{\alpha}^{\text{eq}}\right) \tag{A.38}$$

and a corresponding concentration normal vector \hat{n}_c by

$$\hat{n}_c = \frac{\Delta \vec{C}_{\text{eq}}^{\alpha}}{|\Delta \vec{C}_{\text{eq}}^{\alpha}|} \tag{A.39}$$

where | | denotes the usual vector norm (and $|\hat{n}_c| = 1$). In terms of Eq. (A.38) and Eq. (A.39), Eq. (A.37) can be written the more compact form

$$\omega^{\alpha}(\vec{\mu}) - \omega^{L}(\vec{\mu}) = |\Delta \vec{C}_{\text{eq}}^{\alpha}|^{2} \left\{ \vec{U}_{\alpha}^{T} \frac{(\boldsymbol{I} - [\boldsymbol{K}^{\alpha}])}{2} + \hat{n}_{c}^{T} \right\} [\boldsymbol{\chi}^{L}]^{-1} \vec{U}_{\alpha}$$
(A.40)

Equation (A.40) is exactly the matrix analogue of the driving force used in the binary alloy phase field equations in previous sections, except that here it is applicable to multiple components.

Final form of phase field equations in terms of supersaturation vector

We summarize here the various expressions from the previous sub-sections to compile the final form of the phase field equations of motions. We state the equations first, followed by a summary of the expression that are required to evaluate the various expressions that go into the evolution equations.

The dynamical evolution equations for each order parameter and for the chemical potential (corrected by anti-trapping) become,

$$\tau_{\alpha} \frac{\partial \phi_{\alpha}}{\partial t} = W_{\alpha}^{2} \nabla^{2} \phi_{\alpha} - f_{\text{DW}}'(\phi_{\alpha}) - w_{obs} \phi_{\alpha} \sum_{\beta \neq \alpha}^{N} \phi_{\beta}^{2} - \left(\frac{(\boldsymbol{I} - [\boldsymbol{K}^{\alpha}])^{T}}{2} \vec{U}_{\alpha} + \hat{n}_{c} \right)^{T} [\lambda_{\alpha}] \vec{U}_{\alpha} g_{\alpha}'(\boldsymbol{\phi})$$
(A.41)

and

$$[\boldsymbol{\chi}] \frac{\partial \vec{\mu}}{\partial t} = \boldsymbol{\nabla} \cdot \left[[\boldsymbol{M}] \boldsymbol{\nabla} \vec{\mu} + \sum_{\alpha} W_{\alpha} a(\boldsymbol{\phi}) |\Delta \vec{C}_{eq}^{\alpha}| \left\{ \hat{n}_{c} + (\boldsymbol{I} - [\boldsymbol{K}^{\alpha}])^{T} \vec{U}_{\alpha} \right\} \frac{\partial \phi_{\alpha}}{\partial t} \frac{\boldsymbol{\nabla} \phi_{\alpha}}{|\boldsymbol{\nabla} \phi_{\alpha}|} \right] + \frac{1}{2} \sum_{\alpha} |\Delta \vec{C}_{eq}^{\alpha}| \left\{ \hat{n}_{c} + (\boldsymbol{I} - [\boldsymbol{K}^{\alpha}])^{T} \vec{U}_{\alpha} \right\} \frac{\partial \phi_{\alpha}}{\partial t},$$
(A.42)

where

$$\vec{U}_{\alpha} = \frac{\left[\chi^{L}\right]}{\left|\Delta\vec{C}_{\text{eq}}^{\alpha}\right|} \left(\vec{\mu} - \vec{\mu}_{\alpha}^{\text{eq}}\right) \tag{A.43}$$

$$\hat{n}_c = \frac{\Delta \vec{C}_{\text{eq}}^{\alpha}}{|\Delta \vec{C}_{\text{eq}}^{\alpha}|} \tag{A.44}$$

$$[\mathbf{K}^{\alpha}] = [\mathbf{\chi}^L]^{-1} [\mathbf{\chi}^{\alpha}] \tag{A.45}$$

$$[\lambda_{\alpha}] = \hat{\lambda}_{\alpha} |\Delta \vec{C}_{eq}^{\alpha}|^2 [\chi^L]^{-1}$$
(A.46)

$$\Delta \vec{C}_{\rm eq}^{\alpha} = \vec{c}_{\rm eq}^{\ L} - \vec{c}_{\rm eq}^{\ \alpha} \tag{A.47}$$

$$[\boldsymbol{\chi}] = [\boldsymbol{\chi}^L] \left\{ \mathbf{I} - \sum_{\alpha} \left(\mathbf{I} - [\boldsymbol{K}^{\alpha}] \right) h_{\alpha}(\vec{\phi}) \right\}$$
(A.48)

$$[\boldsymbol{M}] = \sum_{\alpha}^{N} q_{\alpha}(\boldsymbol{\phi}) [\boldsymbol{D}]^{\alpha} [\boldsymbol{\chi}^{\alpha}] + \left(1 - \sum_{\alpha}^{N} q_{\alpha}(\boldsymbol{\phi})\right) [\boldsymbol{D}^{L}] [\boldsymbol{\chi}^{L}]$$
(A.49)

The outer gradient operator in Eq. (A.42) contracts with the index of the inner gradients for the first and second terms on the right hand side of Eq. (A.42). The matrices $[\chi^L]$ and $[\chi^{\alpha}]$ are given by Eq. (A.5). The other parameters, τ_{α} , W_{α} w_{obs} , as well as the interpolation functions are as defined in the previous sections. It is clear that equations Eq. (A.41) and Eq. (A.42) are precisely the vector analogues of Eq. (2.55) and Eq. (2.51), and in the special case of a single component and single order parameter, these equations collapse back to equations Eq. (2.59) and Eq. (2.60).

It is noted that the evolution of each order parameter ϕ_{α} is driven by the entire vector of reduced supersaturations in \vec{U}_{α} . Also, the are there are as many \vec{U}_{α} as there are distinct solid phases, since they represent the differences in chemical potentials relative to the equilibrium chemical potential of each phase (α) .

In the above model, the susceptibility matrix $[\chi]$ and [M] need to be evaluated at each point in space, $[\chi^L]^{-1}$, $[\chi^{\alpha}]$ and $[K^{\alpha}]$ need only be computed once. However, for a more robust description of realistic alloys, the coefficient matrices in the equations of motion should be made $\vec{\mu}$ (or \vec{c}) dependent, thus adopting changing values that

76 A Phase Field Dynamics for General Complex Alloy Systems

can better capture the properties of liquid and solid over different broad ranges of concentration space that can occur in the system.

B

Incorporating Temperature

The consideration of non-isothermal conditions can be readily described as well. In order to do so, we re-write the grand potential functional to explicitly consider temperature. We have

$$\Omega[\boldsymbol{\phi}, \boldsymbol{\mu}, T] = \int_{V} \left\{ \omega_{\text{int}} \left(\boldsymbol{\phi}, \boldsymbol{\nabla} \boldsymbol{\phi} \right) + \sum_{\alpha}^{N} g_{\alpha}(\boldsymbol{\phi}) \omega^{\alpha}(\boldsymbol{\mu}, T) + \left[1 - \sum_{\alpha}^{N} g_{\alpha}(\boldsymbol{\phi}) \right] \omega^{\ell}(\boldsymbol{\mu}, T) \right\},$$
(B.1)

where we have neglected the temperature (T) dependence on the interaction part of the functional. Strictly speaking, the surface term, energy barrier height, and grain interaction constants in ω_{int} should include some temperature dependence. However, these constants will be assumed for simplicity to be independent of temperature.

Temperature evolution is derived by considering the conservation the transport of internal energy e, which written as,

$$\frac{\partial e}{\partial t} = \mathbf{\nabla} \left(k(\boldsymbol{\phi}, T) \mathbf{\nabla} T \right), \tag{B.2}$$

where $k(\phi, T)$ is the transport coefficient, i.e., the heat conductivity. The energy can be eliminated in favour of temperature through the generalized entropy density, which is given by the variational of the grand potential with temperature,

$$s = -\frac{\delta\Omega[\phi, \mu, T]}{\delta T}.$$
 (B.3)

The variation of the functional becomes

$$\delta\Omega = \int_{V} \left(\left\{ -\sigma_{\alpha} \nabla^{2} \phi_{\alpha} + H_{\alpha} f_{\text{DW}}^{\prime}(\phi_{\alpha}) + \sum_{\beta \neq \alpha} \Psi^{\prime}(\phi_{\alpha}, \phi_{\beta}) + g_{\alpha}^{\prime}(\phi) \left[\omega^{\alpha}(\boldsymbol{\mu}, T) - \omega^{\ell}(\boldsymbol{\mu}, T) \right] \right\} \delta\phi_{\alpha}$$

$$+ \sum_{i} \left\{ \sum_{\alpha}^{N} g_{\alpha}(\phi) \frac{\partial \omega^{\alpha}(\boldsymbol{\mu}, T)}{\partial \mu_{i}} + \left[1 - \sum_{\alpha}^{N} g_{\alpha}(\phi) \right] \frac{\partial \omega^{\ell}(\boldsymbol{\mu}, T)}{\partial \mu_{i}} \right\} \delta\mu_{i}$$

$$+ \left\{ \sum_{\alpha}^{N} g_{\alpha}(\phi) \frac{\partial \omega^{\alpha}(\boldsymbol{\mu}, T)}{\partial T} + \left[1 - \sum_{\alpha}^{N} g_{\alpha}(\phi) \right] \frac{\partial \omega^{\ell}(\boldsymbol{\mu}, T)}{\partial T} \right\} \delta T \right) d^{3}\boldsymbol{r} \qquad (B.4)$$

Considering the temperature variation, we have

$$s(\boldsymbol{\phi}, \boldsymbol{\mu}, T) = -\left\{ \sum_{\alpha}^{N} g_{\alpha}(\boldsymbol{\phi}) \frac{\partial \omega^{\alpha}(\boldsymbol{\mu}, T)}{\partial T} + \left[1 - \sum_{\alpha}^{N} g_{\alpha}(\boldsymbol{\phi}) \right] \frac{\partial \omega^{\ell}(\boldsymbol{\mu}, T)}{\partial T} \right\}, \quad (B.5)$$

which can be cast into the form

$$s(\boldsymbol{\phi}, \boldsymbol{\mu}, T) = \sum_{\alpha}^{N} g_{\alpha}(\boldsymbol{\phi}) s^{\alpha}(\boldsymbol{\mu}, T) + \left[1 - \sum_{\alpha}^{N} g_{\alpha}(\boldsymbol{\phi}) \right] s^{\ell}(\boldsymbol{\mu}, T), \tag{B.6}$$

where we have used $s^{\vartheta} = -\partial \omega^{\vartheta}/\partial T$, the entropy density for a particular phase. The s^{ϑ} define *auxiliary* entropy fields in the same sense as the auxiliary concentration fields. Using the thermodynamic relation de = Tds, which is valid at constant pressure, we have

$$\frac{\partial e}{\partial t} = T \frac{\partial s}{\partial t}
= T \left(\sum_{\alpha}^{N} \frac{\partial s}{\partial \phi_{\alpha}} \frac{\partial \phi_{\alpha}}{\partial t} + \sum_{i} \frac{\partial s}{\partial \mu_{i}} \frac{\partial \mu_{i}}{\partial t} + \frac{\partial s}{\partial T} \frac{\partial T}{\partial t} \right).$$
(B.7)

We readily identify the specific heat capacity, c_p , from the above equation as being

$$c_{p}(\boldsymbol{\phi}, \boldsymbol{\mu}, T) = T \frac{\partial s}{\partial T}$$

$$= \sum_{\alpha}^{N} g_{\alpha}(\boldsymbol{\phi}) c_{p}^{\alpha}(\boldsymbol{\mu}, T) + \left[1 - \sum_{\alpha}^{N} g_{\alpha}(\boldsymbol{\phi})\right] c_{p}^{\ell}(\boldsymbol{\mu}, T), \tag{B.8}$$

while the other derivatives in the expression are

$$\frac{\partial s(\boldsymbol{\phi}, \boldsymbol{\mu}, T)}{\partial \mu_i} = \sum_{\alpha}^{N} g_{\alpha}(\boldsymbol{\phi}) \frac{\partial s^{\alpha}(\boldsymbol{\mu}, T)}{\partial \mu_i} + \left[1 - \sum_{\alpha}^{N} g_{\alpha}(\boldsymbol{\phi}) \right] \frac{\partial s^{\ell}(\boldsymbol{\mu}, T)}{\partial \mu_i}, \tag{B.9}$$

and

$$\frac{\partial s(\boldsymbol{\phi}, \boldsymbol{\mu}, T)}{\partial \phi_{\alpha}} = \sum_{\alpha}^{N} g_{\alpha}'(\boldsymbol{\phi}) \left[s^{\alpha}(\boldsymbol{\mu}, T) - s^{\ell}(\boldsymbol{\mu}, T) \right], \tag{B.10}$$

The evolution equation for temperature now reads

$$\frac{\partial T}{\partial t} = \frac{1}{c_p(\boldsymbol{\phi}, \boldsymbol{\mu}, T)} \left[\boldsymbol{\nabla} \cdot k(\boldsymbol{\phi}, T) \boldsymbol{\nabla} T - T \sum_{\alpha}^{N} g_{\alpha}'(\boldsymbol{\phi}) \left[s^{\alpha}(\boldsymbol{\mu}, T) - s^{\ell}(\boldsymbol{\mu}, T) \right] \frac{\partial \phi_{\alpha}}{\partial t} \right.$$

$$- T \sum_{i}^{n-1} \left(\sum_{\alpha}^{N} g_{\alpha}(\boldsymbol{\phi}) \frac{\partial s^{\alpha}(\boldsymbol{\mu}, T)}{\partial \mu_i} + \left[1 - \sum_{\alpha}^{N} g_{\alpha}(\boldsymbol{\phi}) \right] \frac{\partial s^{\ell}(\boldsymbol{\mu}, T)}{\partial \mu_i} \right) \frac{\partial \mu_i}{\partial t} \right]. \quad (B.11)$$

The concept of anti-trapping current can also be considered for temperature as latent heat can also be trapped. This effect was initially studied by Almgren for solidification of a pure material [60] where different thermal diffusivities were considered. However, since the time scale of solute diffusion is orders of magnitude slower than temperature diffusion, we believe that this will not be necessary

The order parameter equation remains the same, aside from including some temperature dependence, i.e.,

$$\frac{\partial \phi_{\alpha}}{\partial t} = M_{\phi_{\alpha}} \left[\sigma_{\alpha} \nabla^{2} \phi_{\alpha} - H_{\alpha} f'_{\text{DW}}(\phi_{\alpha}) - \sum_{\beta \neq \alpha} \Psi'(\phi_{\alpha}, \phi_{\beta}) - g'_{\alpha}(\phi) \left[\omega^{\alpha}(\boldsymbol{\mu}, T) - \omega^{\ell}(\boldsymbol{\mu}, T) \right] \right].$$
(B.12)

The evolution of chemical potential, including anti-trapping, now reads

$$\frac{\partial \mu_{i}}{\partial t} = \frac{1}{\chi(\boldsymbol{\phi}, \mu_{i}, T)} \left\{ \boldsymbol{\nabla} \cdot \left[\sum_{j} M_{ij}(\boldsymbol{\phi}, T) \boldsymbol{\nabla} \mu_{i} + \sum_{\alpha} a(\boldsymbol{\phi}) W \left[c_{i}^{\ell}(\boldsymbol{\mu}, T) - c_{i}^{\alpha}(\boldsymbol{\mu}, T) \right] \frac{\partial \phi_{\alpha}}{\partial t} \frac{\boldsymbol{\nabla} \phi_{\alpha}}{|\boldsymbol{\nabla} \phi_{\alpha}|} \right] \right. \\
\left. - \sum_{\alpha} h_{\alpha}'(\boldsymbol{\phi}) \left[c_{i}^{\alpha}(\boldsymbol{\mu}, T) - c_{i}^{\ell}(\boldsymbol{\mu}, T) \right] \frac{\partial \phi_{\alpha}}{\partial t} - \left(\sum_{\alpha}^{N} h_{\alpha}(\boldsymbol{\phi}) \frac{\partial c_{i}^{\alpha}(\boldsymbol{\mu}, T)}{\partial T} + \left[1 - \sum_{\alpha}^{N} h_{\alpha}(\boldsymbol{\phi}) \right] \frac{\partial c_{i}^{\ell}(\boldsymbol{\mu}, T)}{\partial T} \right) \frac{\partial T}{\partial t} \right\} \tag{B.13}$$

In the case of quadratic free energy fittings, i.e. like in section 2.6 and 3.1, if the fitting scheme is well defined at each temperature, it is reasonable to assume one can just interpolate between parabolic fitting parameters to induce a cooling rate in the simulation. However, spurious kinetics may arise if the parameters change dramatically between temperature indices and the interpolation scheme doesn't accurately capture this. In general, at low rates of solidification such effects negligible in theory, but worth investigating.

- [1] Mathis Plapp. Unified derivation of phase-field models for alloy solidification from a grand-potential functional. *Phys. Rev. E*, 84:031601, 2011.
- [2] KA Jackson and JD Hunt. Lamellar and rod eutectic growth. AIME Met Soc Trans, 236:1129–1142, 1966.
- [3] Nana Ofori-Opoku and Nikolas Provatas. A quantitative multi-phase field model of polycrystalline alloy solidification. *Acta Materialia*, 58(6):2155 2164, 2010.
- [4] C. Tong, M. Greenwood, and N. Provatas. Phys. Rev. E, 77:1, 2008.
- [5] J. B. Collins and H. Levine. *Phys. Rev. B*, 31:6119, 1985.
- [6] P. C. Hohenberg and B. I. Halperin. Rev. Mod. Phys., 49:435, 1977.
- [7] A. Karma and W. J. Rappel. Quantitative phase-field modeling of dendritic growth in two and three dimensions. *Phys. Rev. E*, 57:4323–4349, 1998.
- [8] J.S. Langer. Rev. Mod. Phys., 52:1, 1980.
- [9] G. Caginalp and E. Socolovsky. SIAM J. Sci. Comp., 15:106, 1991.
- [10] N Provatas, N Goldenfeld, and J Dantzig. Efficient computation of dendritic microstructures using adaptive mesh refinement. *Phys. Rev. Lett.*, 80:3308–3311, 1998.
- [11] N. Provatas, J. Dantzig, and N. Goldenfeld. J. Comp. Phys., 148:265, 1999.
- [12] J. A. Warren and W. J. Boettinger. Acta Metall. Mater. A, 43:689, 1995.
- [13] A. Karma. Phys. Rev. Lett, 87:115701, 2001.

[14] B. Echebarria, R. Folch, A. Karma, and M. Plapp. Phys. Rev. E., 70:061604–1, 2004.

- [15] J. C. Ramirez, C. Beckermann, A. Karma, and H. J. Diepers. *Phys. Rev. E*, 69:051607, 2004.
- [16] A. G. Khachaturyan. Theory of structural transformations in solids. Wiley-Interscience Publications (New York), 1983.
- [17] K. R. Elder, Zhi-Feng Huang, and Nikolas Provatas. Amplitude expansion of the binary phase-field-crystal model. *Phys. Rev. E*, 81:011602, Jan 2010.
- [18] Zhi-Feng Huang, K. R. Elder, and Nikolas Provatas. Phase-field-crystal dynamics for binary systems: Derivation from dynamical density functional theory, amplitude equation formalism, and applications to alloy heterostructures. *Phys. Rev. E*, 82:021605, Aug 2010.
- [19] Kuo-An Wu, Ari Adland, and Alain Karma. Phase-field-crystal model for fcc ordering. *Phys. Rev. E*, 81:061601, 2010.
- [20] Nana Ofori-Opoku, Jonathan Stolle, Zhi-Feng Huang, and Nikolas Provatas. Complex order parameter phase-field models derived from structural phase-field-crystal models. *Phys. Rev. B*, 88:104106, Sep 2013.
- [21] L. Q. Chen and W. Yang. Phy. Rev. B, 50:15752, 1994.
- [22] A. Kazaryan, Y. Wang, S. A. Dregia, and B. R. Patton. Phys. Rev. B, 61:14275, 2000.
- [23] D. Fan, S. P. Chen, L.-Q. Chen, and P. W. Voorhees. *Acta Materialia*, 50:1897, 2002.
- [24] J. Z. Zhu, T. Wang, A. J. Ardell, S. H. Zhou, Z. K. Lui, and L. Q. Chen. Acta Materialia, 52:2837, 2004.

[25] J. Zhu, T. Wang, S. Zhou, Z. Liu, and L.-Q. Chen. Acta Materialia, 52:833, 2004.

- [26] Nele Moelans. Acta materialia, 59:1077, 2011.
- [27] J. Tiaden, B. Nestler, H. Diepers, and I. Steinbach. *Physica D*, 115:73, 1998.
- [28] S. G. Kim, W. T. Kim, and T. Suzuki. *Phys. Rev. E*, 60:7186, 1999.
- [29] S. G. Kim. Acta Materialia, 55:4391, 2007.
- [30] C. Shen, Q. Chen, Y. H. Wen, J. P. Simmons, and Y. Wang. *Scripta Materialia*, 50(7):1023 1028, 2004.
- [31] N. Moelans, B. Blanpain, and P. Wollants. *Phys Rev Lett*, 101(025502), 2008.
- [32] N. Moelans, B. Blanpain, and P. Wollants. Phy. Rev. B, 78:024113, 2008.
- [33] B. Morin, K.R. Elder, M. Sutton, and M. Grant. Phys. Rev. Lett., 75:2156, 1995.
- [34] R. Kobayashi, J. A. Warren, and W. C. Carter. *Physica D*, 119:415, 1998.
- [35] R. Kobayashi, J. A. Warren, and W. C. Carter. *Physica D.*, 140:141, 2000.
- [36] R. Kobayashi and J. A. Warren. *Physica A*, 356:127, 2005.
- [37] L. Gránásy, T. Pusztai, and J. A. Warren. J. Phys.: Condens. Matter, 16:R1205, 2004.
- [38] Badrinarayan P. Athreya, Nigel Goldenfeld, Jonathan A. Dantzig, Michael Greenwood, and Nikolas Provatas. Adaptive mesh computation of polycrystalline pattern formation using a renormalization-group reduction of the phase-field crystal model. *Phys. Rev. E*, 76:056706, Nov 2007.
- [39] I. Steinbach, F. Pezzolla, B. Nestler M. Seebelberg, R. Prieler, and G. J. Schmitz. Physica D, 94:135, 1999.
- [40] H. Garcke, B. Nestler, and B. Stoth. SIAM J. Appl. Math, 60:295, 1999.

[41] B. Nestler, H. Garcke, and B. Stinner. Phys. Rev. E, 71:041609–1, 2005.

- [42] B. Bottger and I. Steinbach. Acta Materialia, 54:2697, 2006.
- [43] I. Steinbach. Apel M. Physica D, 217:153, 2006.
- [44] J. Eiken, B. Böttger, and I. Steinbach. Phys Rev E, 73:066122, 2006.
- [45] I. Steinbach. Modelling Simul. Mater. Sci. Eng., 17:073001, 2009.
- [46] Nikolas Provatas and Ken Elder. *Phase-Field Methods in Materials Science and Engineering*. Wiley-VCH Verlag GmbH & Co. KGaA, 2010.
- [47] R. Folch and M. Plapp. Phys. Rev. E., 72:011602, 2005.
- [48] A. Choudhury and B. Nestler. Phys. Rev. E, 85:021602, 2012.
- [49] Johannes Hotzer, Marcus Jainta, Philipp Steinmetz, Britta Nestler, Anne Dennstedt, Amber Genau, Martin Bauer, Harald Kostlerc, and Ulrich Rudec. Large scale phase-field simulations of directional ternary eutectic solidification. Acta Materialia, 93:194, 2015.
- [50] B Nestler and AA Wheeler. A multi-phase-field model of eutectic and peritectic alloys: numerical simulation of growth structures. *Physica D: Nonlinear Phenomena*, 138(1):114–133, 2000.
- [51] Jonathan A Dantzig and Michel Rappaz. Solidification. EPFL press, 2009.
- [52] Martin Grant. Dirty tricks for statistical mechanics: time dependent things. Lecture Notes for Advanced Statistical Physics, Version 0.8, August 2005.
- [53] Jan-Olof Andersson and John Agren. Models for numerical treatment of multicomponent diffusion in simple phases. *J. Appl. Phys.*, 72(4):1350, 1992.
- [54] Kuo-An Wu and Alain Karma. Phase-field crystal modeling of equilibrium bcc-liquid interfaces. *Phys. Rev. B*, 76:184107, Nov 2007.

[55] Sami Majaniemi and Nikolas Provatas. Deriving surface-energy anisotropy for phenomenological phase-field models of solidification. *Phys. Rev. E*, 79(1):011607, 2009.

- [56] Nikolas Provatas and Sami Majaniemi. Phase-field-crystal calculation of crystal-melt surface tension in binary alloys. *Phys. Rev. E*, 82(4):041601, 2010.
- [57] Hao Zhang, David J. Srolovitz, Jack F. Douglas, and James A. Warren. *PNAS*, 106(19):7735, 2009.
- [58] G. Caginalp and P. C. Fife. Phys. Rev. B, 11:7792, 1986.
- [59] G. Caginalp. Phys. Rev. A, 39:5887, 1989.
- [60] R. Almgren. SIAM J. Appl. Math., 59:2086, 1999.
- [61] Q. Bronchart, Y. Le Bouar, and A. Finel. Phys Rev Lett, 100:015702, 2008.
- [62] Chakin and Lubensky. Principles of Condensed Matter Physics, page 629. North Holland, Amsterdam, 1987.
- [63] A. Karma and W.-J. Rappel. Phys. Rev. E, 60:3614, 1999.
- [64] Blas Echebarria, Alain Karma, and Sebastian Gurevich. Phys. Rev. E, 81:021608, 2010.
- [65] Chaohui Tong, Michael Greenwood, and Nikolas Provatas. Quantitative phase-field modeling of solidification in binary alloys with nonlinear phase coexistence curves. *Physical Review B*, 77(6):064112, 2008.
- [66] R.C. Brower, D. Kessler, J. Koplik, and H. Levine. Phys. Rev. Lett., 51:1111, 1983.
- [67] E. Ben-Jacob, N. Goldenfeld, J.S. Langer, and G. Schön. Phys. Rev. Lett., 51:1930, 1983.

[68] E. Ben-Jacob, N. Goldenfeld, B. G. Kotliar, and J. S. Langer. Phys. Rev. Lett., 53:2110, 1984.

- [69] D. Kessler J. Koplik and H. Levine. *Phys. Rev. A*, 30:3161, 1984.
- [70] D. A. Kessler and H. Levine. *Phys. Rev. A.*, 39:3041, 1989.
- [71] E. Brener and V. I. Melnikov. Adv. Phys., 40:53, 1991.
- [72] Y. Pomeau and M. Ben Amar. *Solids far from equilibrium*, page 365. edited by by C. Godreche, (Cambridge Press), 1991.
- [73] D Tourret and A Karma. Growth competition of columnar dendritic grains: A phase-field study. *Acta Materialia*, 82:64–83, 2015.
- [74] Jihene Ghmadh, Jean-Marc Debierre, Julien Deschamps, Marc Georgelin, Rahma Guérin, and Alain Pocheau. Directional solidification of inclined structures in thin samples. Acta Materialia, 74:255–267, 2014.
- [75] Alain Karma and Wouter-Jan Rappel. Phase-field model of dendritic sidebranching with thermal noise. *Physical review E*, 60(4):3614, 1999.
- [76] J. Heulens, B. Blanpain, and N. Moelans. Acta materialia, 59:2156, 2011.